

# Advanced numerical modelling of caisson foundations in sand to investigate the failure envelope in the $H$ - $M$ - $V$ space

Zhuang JIN<sup>a,b</sup>, Zhen-Yu YIN<sup>a,\*</sup>, Panagiotis KOTRONIS<sup>b</sup> and Zheng LI<sup>c</sup>

<sup>a</sup> Department of Civil and Environmental Engineering, The Hong Kong Polytechnic University, Hung Hom, Kowloon, Hong Kong, China

<sup>b</sup> École Centrale de Nantes, Université de Nantes, CNRS, Institut de Recherche en Génie Civil et Mécanique (GeM), UMR 6183, 1 rue de la Noë, BP 92101, 44321, Nantes, cedex 3, France

<sup>c</sup> IFSTTAR, GERS, GMG, Bouguenais, France

\* Corresponding author: Dr Zhen-Yu Yin, Tel. +852 34008470, Fax +852 23346389, Email: [zhenyu.yin@polyu.edu.hk](mailto:zhenyu.yin@polyu.edu.hk); [zhenyu.yin@gmail.com](mailto:zhenyu.yin@gmail.com)

**Abstract:** This paper focuses on the identification of the failure envelope of a caisson foundation in sand using an advanced critical state-based sand model (SIMSAND) and the Combined Lagrangian Smoothed Particle Hydrodynamics Method (CLSPH). The parameters of the SIMSAND constitutive model are first calibrated using triaxial tests on Baskarp sand. In order to validate the combined CLSPH-SIMSAND approach, a cone penetration test, model tests and a field test on a reduced scale caisson foundation are simulated. After full numerical validations with different scales from laboratory to in-situ conditions, a numerical parametrical study is then introduced considering different sand properties (density, friction angle, deformability, crushability) and caisson dimensions (soil-structure contact surface area, diameter-depth ratio) and complex combined loading paths to identify the failure envelope in the horizontal force ( $H$ ), bending moment ( $M$ ), vertical force ( $V$ ) space. The influence of the caisson foundation contact surface area, aspect ratio and soil parameters are considered and quantified. Finally, an analytical formula is proposed for the 3D failure envelope in the  $H$ - $M$ - $V$  space.

**Keywords:** Failure envelope; suction bucket foundation; sand; critical state; Smoothed Particle Hydrodynamics Method; constitutive model

# 1 Introduction

The design of caisson foundations has recently become an important geotechnical challenge. Although caisson foundations have been used in the oil and gas industry for several decades (Tjelta, 1995; 2001), they have been used for Offshore Wind Turbines (OWT) since the early 21<sup>st</sup> century (Houlsby et al., 2005; Houlsby et al., 2006; Iskander et al., 2002; Nguyen-Sy and Houlsby, 2005; Senders, 2009; Villalobos et al., 2009; Villalobos et al., 2004). Providing a skirt, caisson foundations significantly improve the stiffness and the bearing capacity with the additional expense of a (minor) weight increase compared to classical surface foundations (Villalobos et al., 2003). A caisson foundation is lighter than a gravity platform jacket; nevertheless, the horizontal loads and moments are high in comparison to its weight.

For an optimum caisson foundation design in the offshore field it is necessary to consider the couplings between the vertical force ( $V$ ), the horizontal force ( $H$ ) and the bending moment ( $M$ ). Previous research studies on the bearing capacity of caisson foundations in sand mainly focused in in-situ tests (Hogervorst, 1980; Houlsby et al., 2006; Tjelta, 1995), model test (Byrne and Houlsby, 2001; Cassidy et al., 2002; Foglia et al., 2015; Gottardi et al., 1999; Ibsen et al., 2013; Ibsen et al., 2014) or finite element method simulations (Gerolymos et al., 2015; Liu et al., 2014; Zafeirakos and Gerolymos, 2016; Jin et al., 2018b). The above experimental or numerical results can be used to construct simplified numerical strategies for design purposes, e.g. macroelements (Byrne and Houlsby, 2001; Cassidy et al., 2002; Cremer et al., 2001; Gottardi et al., 1999; Grange et al., 2008; Li et al., 2016; Montrasio and Nova, 1997; Nova and Montrasio, 1991; Salciarini and Tamagnini, 2009). Following the macroelement concept, the entire soil-foundation system is regarded as a single element with a constitutive law expressed in generalised variables following the plasticity or hypoplasticity theory. Compared to a conventional finite element approach,

1 macroelements are simpler, faster and more robust but suitable only for specific foundation -  
2 soil configurations.  
3  
4

5 The definition of the failure surface is of paramount importance in the development a  
6 macroelement (Gottardi and Butterfield, 1993; Gourvenec and Barnett, 2011; Gourvenec and  
7 Randolph, 2003; Houlsby and Cassidy, 2002; Li et al., 2014) as it introduces the effects of  
8 combined loads for different loading levels. An investigation of the failure surface entirely  
9 based on model tests induces however important financial and computational costs (Byrne,  
10 2000; Foglia et al., 2015; Ibsen et al., 2013; Nguyen-Sy, 2005; Villalobos et al., 2010). A  
11 timesaving and more economical approach is to use a combination of experiments and finite  
12 element method simulations. It is worth noting however that the reliability of the numerical  
13 analysis depends on its ability to realistically reproduce the soil nonlinear behaviour.  
14  
15  
16  
17  
18  
19  
20  
21  
22  
23  
24  
25  
26  
27

28 The response of a caisson foundation in sand subjected to combined loading has been  
29 recently simulated with different constitutive models, such as a plasticity constitutive model  
30 governed by the Mohr-Coulomb failure criterion (Achmus et al., 2013; Liu et al., 2014;  
31 Zafeirakos and Gerolymos, 2016), the NGI - ADP model with an anisotropic undrained shear  
32 strength failure criterion (Skau et al., 2018) and an elastoplasticity model called Hardening  
33 Small strain Soil model (HSS) which can reproduce basic macroscopic phenomena in the soil  
34 (Li et al., 2015). The calibration strategy of the soil parameters is also of great importance.  
35 Some studies adopt back calculations from experimental field tests or empirical formulas  
36 (Achmus et al., 2013; Zafeirakos and Gerolymos, 2016), the representative soil strength  
37 profile of specific areas when the relevant soil parameters are not available (Liu et al., 2014;  
38 Skau et al., 2018) or triaxial tests and back analysis using the finite element method (Li et al.,  
39 2015). However, the full numerical analyses with different scales from laboratory to in-situ  
40  
41  
42  
43  
44  
45  
46  
47  
48  
49  
50  
51  
52  
53  
54  
55  
56  
57  
58  
59  
60  
61  
62  
63  
64  
65

conditions including large deformation phases (e.g. CPT or caisson penetration for validations) have not been reported.

The Combined Lagrangian-SPH method (CLSPH) is adopted hereafter to take into account large deformations. The study focuses on the condition of a regular wave loading with the frequency usually varying from 0.2 to 0.35 Hz. For the case of sand foundation which is highly permeable, it is reasonable to consider a drained condition for the design. The SIMSAND critical state elastoplastic constitutive model is used to describe in a realistic way the sand characteristics, the evolving failure envelope and the influence of different soil parameters (density, friction angle, deformability and grain crushability). The SIMSAND soil parameters are calibrated from triaxial tests on Baskarp sand. The CLSPH-SIMSAND numerical model is then validated using a cone penetration test, model tests and a reduced scale field test. A large number of finite element simulations are then carried out to investigate the behaviour of a caisson foundation in sand subjected to different load combinations. In order to identify the failure envelope in the  $H$ - $M$ - $V$  space, radial displacement loadings are applied. Various factors affecting the shape and size of the failure envelope are considered, including soil density, friction strength, soil stiffness, grain breakage, foundation geometry and aspect ratio. The coupling relationships among geometry, aspect ratio and characteristic parameters of the failure envelope are quantified with a general equation. An analytical formula of the 3D failure surface is finally proposed, useful for design purposes and the development of macroelements.

## **2 CLSPH - SIMSAND numerical modeling strategy**

### **2.1 The Combined Lagrangian - SPH method (CLSPH)**

The Smooth Particle Hydrodynamics (SPH) method was initially developed by Gingold and Monaghan (1977) for numerical analysis in the field of astrophysics. Further

developments allowed for applications in solid mechanics. In the SPH method, the computational domain is modelled by a set of discrete particles. The particles have a kernel function to determine their interaction range, which is called the influence domain. Each particle has a volume and a mass and carries several properties such as acceleration, velocity, void ratio etc. (Chen and Qiu, 2012). The interpolation process is based on the following integral representation of a field function  $f(x)$ :

$$f(x) = \int_{\Omega} f(x') W(x-x', h) dx' \quad (1)$$

where  $x$  represents the location of the particle;  $\Omega$  is the influence domain of the integral;  $W$  is the basis function of the approximation, also called the kernel or smoothing function; and  $h$  is the smoothing length, which controls the influence domain of  $W$ .  $f(x)$  is further approximated by the summation over neighbouring particles as follows:

$$f(x) = \sum_{i=1}^N f(x_i) W(x-x_i, h) V_i = \sum_{i=1}^N f(x_i) W(x-x_i, h) \frac{m_i}{\rho_i} \quad (2)$$

where  $V_i$ ,  $\rho_i$  and  $m_i$  represent the volume, density and mass of the particle  $i$  respectively;  $N$  is the number of influencing particles. The spatial derivative of  $f(x)$  is approximated by differential operations on the smoothing function:

$$\frac{\partial f(x)}{\partial x} = \sum_{i=1}^N \frac{m_i}{\rho_i} f(x_i) \frac{\partial W(x-x_i, h)}{\partial x_i} \quad (3)$$

The efficiency and accuracy of the SPH method depend on the kernel function. The particles are used as interpolation points to estimate all variables in a continuum. Great distances can separate the SPH particles and the variables between the particles can be approximated by smoothing shape functions. When a particle reaches a certain distance, called smoothing length  $h$ , from another particle, the two particles start to interact. A

1 smoother or more continuous behaviour can therefore be achieved with a larger smoothing  
2 length. On the contrary, a smaller smoothing length results in a more discrete behaviour.  
3  
4

5 The major advantage of the SPH method is that there is no need for a fixed  
6 computational grid when calculating spatial derivatives. An analytical expression based on  
7 the derivative of the smoothing function can be used instead (Li and Liu, 2002). Since the  
8 particles interact, the SPH method can deal with very large deformations. The SPH method is  
9 complementary approach with respect to the Arbitrary Lagrangian Euler (ALE) method. The  
10 ALE method relies on physically meshing the environment and tends to be more cumbersome  
11 to set up. When the ALE mesh is too distorted to produce good results (for example in the  
12 case of CPT or caisson penetration), SPH is a good alternative method of choice. The coupled  
13 Eulerian-Lagrangian (CEL) method is also a good choice for considering large deformation  
14 on soil-structure interaction. However, the CEL method needs to preset a large Euler domain  
15 according to the calculation basis of CEL method. The Euler mesh should be dense enough so  
16 as to obtain good precision (ABAQUS, 2014). In this study, choosing SPH method costs less  
17 computational resources and has higher calculation efficiency while comparing to CEL.  
18 Comparing to the classical Lagrangian approach, the main disadvantage of the SPH method is  
19 its computational demands (Bojanowski, 2014). It is also less accurate under small  
20 deformations.  
21  
22  
23  
24  
25  
26  
27  
28  
29  
30  
31  
32  
33  
34  
35  
36  
37  
38  
39  
40  
41  
42  
43  
44

45 For all the above reasons, the choice hereafter is discretized only a portion of the  
46 computational domain with the SPH method, while classical Lagrangian finite elements are  
47 used for the remaining (Combined Lagrangian-SPH approach, CLSPH). The CLSPH method  
48 is already implemented into the commercial finite element code ABAQUS. No relative  
49 motion is allowed between the SPH and the Lagrangian domains (via the function “Tie  
50 Constraint”). This allows to fuse the two domains even if the meshes are different. Detailed  
51  
52  
53  
54  
55  
56  
57  
58  
59  
60  
61  
62  
63  
64  
65

information of the CLSPH method can be found in (ABAQUS, 2014).

## 2.2 The critical state soil model SIMSAND

The SIMSAND soil model is based on the Mohr-Coulomb model by implementing the critical state concept (Yin et al. 2017a; Jin et al. 2017) with non-linear elasticity, non-linear plastic hardening and a simplified three-dimensional strength criterion. The state-dependent peak strength and stress-dilatancy (contraction or dilation) are well captured by the SIMSAND model (Jin et al., 2017). The basic constitutive equations of the SIMSAND soil model are summarized in Table 1.

The SIMSAND soil model is implemented into ABAQUS/Explicit as a user-defined material model via a user material subroutine VUMAT and can be used with the CLSPH method. Model implementation follows the work of Hibbitt et al. (2001). In ABAQUS/Explicit, the element strain increment  $\Delta\varepsilon$  at  $\Delta t$  is first given using an explicit time central-differential integration method. Then, the stress increment  $\Delta\sigma$  is updated through the material subroutine VUMAT. The cutting plane algorithm proposed by Ortiz and Simo (1986) is adopted for the stress integration. The SIMSAND model can then be adopted in SPH which was validated by modelling the large deformation of granular collapse (Yin et al., 2018).

In the following, the implementation of the CLSPH-SIMSAND approach is first validated using conventional drained triaxial tests, indoor model tests and a field test.

## 3 Validation of the CLSPH-SIMSAND approach

### 3.1 Drained triaxial tests

The calibration of the constitutive model parameters can be carried out using the straightforward method from experimental results (Wu et al., 2017) or using optimisation methods (Jin et al. 2016a,b; Yin et al. 2016b). In this paper, the experimental results of conventional drained triaxial tests on Baskarp sand (named Aalborg University Sand No 0)

by Houlsby et al. (2005) are used. For the triaxial experiments, three void ratios (0.85, 0.70, 0.61) and nine stress levels (5kPa, 10kPa, 20kPa, 40kPa, 80kPa, 160kPa, 320kPa, 640kPa, 800kPa), 27 groups in total, were tested.

A typical value of Poisson's ratio  $\nu = 0.25$  is assumed. The other two elastic parameters ( $K_0, n$ ) are determined with an isotropic compression test (see Figure 1). The critical state line related parameters  $e_{ref}$ ,  $\lambda$ ,  $\zeta$  are measured from the position of the critical states in the  $p'-e$  plane (Figure 2(d)). Other parameters are calibrated manually from tests on sand with a void ratio  $e_0=0.85$  (Wu et al., 2017). All the calibrated parameters are summarized in Table 2. Using these values, additional tests ( $e_0=0.7, 0.61$ ) are simulated demonstrating the good performance of the model (see Figure 2).

Since the experimental validation of the model covers a wide range from very low level of confining stress (e.g. 5 kPa), the model with identified parameters is applicable for simulating both small scale model tests and real size field tests in Baskarp sand.

## 3.2 Indoor model tests

### 3.2.1 Experimental setup

A well-documented series of laboratory tests of a caisson foundation in sand including the installation phase and the application of monotonic loadings Foglia et al. (2015) is simulated hereafter. The experimental set-up consists of a sand box (1600 mm  $\times$  1600 mm  $\times$  1150 mm), a loading frame and a hinged beam. A system of steel cables and pulleys induces loadings to the foundation through an electric motor drive placed on the hinged beam. The load, set by means of three weight hangers, is transferred to the foundation through a vertical beam bolted on the caisson lid. The foundation is instrumented with three Linear Variable Differential Transformers (LVDTs) and two load cells. The caisson foundation is made of



1 steel, with an outer diameter of 300 mm, a lid thickness of 11.5 mm, a skirt length of 300 mm  
2 and a skirt thickness of 1.5 mm.  
3

4  
5 A Cone Penetration Test (CPT) is first carried out to estimate the soil parameters. Six  
6 tests are then performed under different monotonic loading combinations (one pure vertical  
7 load up to failure and various dimensionally homogeneous moment to horizontal load ratios  
8 ( $M/DH=1.1, 1.987, 3.01, 5.82, 8.748$ ) at constant vertical load).  
9

### 10 11 12 13 14 15 16 17 *3.2.2 Numerical model*

18 The numerical model has the same dimensions as the experimental sand box, see Figure  
19  
20 3. The horizontal displacements of the lateral sides and the translational degrees of freedom  
21 on the bottom are constrained. The main parameters of the finite element model are  
22 summarized in Table 2.  
23  
24  
25  
26

27 In the Combined Lagrangian - SPH model, the part of the soil that experiences large  
28 deformations is modelled with SPH particles (see Figure 3). The SPH domain has a length of  
29 1400 mm at the side where the horizontal or moment loading is applied, a width of 800 mm, a  
30 height of 1150 mm and a total number of 88407 particles. The outer Lagrangian domain is  
31 modelled with 105984 hexahedral elements. The size of SPH domain in the whole model was  
32 examined big enough without boundary effect for all simulations. The SPH domain is densely  
33 covered with SPH particles with an initial particle distance in each direction that remains  
34 approximately constant to obtain a homogenous configuration. The SPH domain interact with  
35 the Lagrangian domain through contact interaction relations defined between a node-based  
36 surface (associated with the particles) and an element-based or analytical surface (ABAQUS,  
37 2014).  
38  
39  
40  
41  
42  
43  
44  
45  
46  
47  
48  
49  
50  
51  
52  
53  
54  
55

56 The caisson has the same size as in the experiment and is modelled with 927 rigid  
57 tetrahedron elements. The density of the steel made caisson is  $7800 \text{ kg/m}^3$ , the Young  
58  
59  
60  
61  
62  
63  
64  
65

modulus 200 GPa and the Poisson ratio 0.3, see Foglia et al. (2015). The caisson is initially located on the soil surface at the centre of the box. For the CPT simulation, the caisson is replaced by a cylinder bar (modelled with 807 rigid tetrahedron elements) with a diameter of 20 mm and a 60 degree cone at the bottom, see Foglia et al. (2015).

### 3.2.3 CPT simulation results

In order to validate the CLSPH-SIMSAND numerical model, the CPT test is simulated hereafter. Following Houlsby et al. (2006), the cone penetration applied velocity is taken equal to 5 mm/s. Assuming a typical soil-structure interface friction coefficient, a rigid Mohr-Coulomb type interface model is adopted and the interface model is applied on the entire (tip and shaft) surface of the cone, see Figure 4(a).

Figure 4(b) presents the simulation results and the comparison with four groups of CPT data, Foglia et al. (2015). Note that an unideal agreement is observed between the simulated CPT penetration and the test for the top 200mm. One possible reason might be the dynamic fluctuation while adopting explicit algorithm. Besides, at the beginning of penetration, due to the tiny size of the pile head, there might be disturbance on the interface between the cone and the soil. As the penetration continues, the trend turned to be similar with the test data. In general, the simulation result indicates that the CLSPH-SIMSAND model with calibrated material parameters performs in an acceptable manner. The plastic deviatoric strain (SDV18), the void ratio (SDV1) and the mean effective stress (S Pressure, kPa) fields corresponding to a penetration of 20mm, 200mm and 400 mm are plotted in Figure 4(c)-(k). The fields of mean effective stress demonstrate clearly the phenomena of cavity expansion with the increase of mean effective stress around the tip of CPT. All results show reasonable distributions with an influence distance much smaller than the SPH domain.

### 3.2.4 Caisson foundation simulation results

The combined Lagrangian - SPH model in Figure 3 is hereafter used to simulate a vertical penetration test with a vertical displacement control at a rate of 5 mm/s, and five tests at various dimensionally homogeneous moment to horizontal load ratios ( $M/DH=1.1, 1.987, 3.01, 5.82, 8.748$ ) at a constant vertical load of 241 N. The horizontal displacements and the rotations are applied at the middle point of the caisson. A relatively slow displacement rate of 10 mm/s and a rotation rate of 0.5 degree/s are chosen to eliminate the dynamic effects. All monotonic loading paths are followed until the vertical bearing capacity ( $VM$ ) or the horizontal capacity and moment capacity ( $MR$ ) are reached.

The applied vertical force versus the vertical displacement for the penetration test is plotted in Figure 5. The results of five typical  $M/DH$  values (1.100, 1.987, 3.010, 5.820 and 8.748) are shown in Figure 6. For all five cases the horizontal load ( $H$ ) versus the horizontal displacement ( $U$ ) and the dimensionally homogeneous moment ( $M/D$ ) versus the rotations ( $D\theta$ ) are plotted. A good agreement is obtained for all tests between experiments and simulations, showing the good performance of the CLSPH-SIMSAND approach.

An extreme case is selected hereafter to check the behaviour of the model under large deformations: the moment horizontal loading test  $M/DH=3.010$ . The plastic deviatoric strain (SDV18), the void ratio (SDV1) and the mean effective stress (S Pressure, kPa) fields at the end of loading are plotted in Figure 7(a)-(c). To further examine the progressive failure, a larger displacement and rotation are applied till the appearance of sliding at the bottom. The corresponding fields of plastic deviatoric strain, void ratio and mean effective stress at large deformation are plotted in Figure 7(d)-(f). All results show reasonable field distributions with an influence distance, in the vertical and horizontal directions, much smaller than the SPH particles domain.

The failure envelopes on the  $H:M/D$  loading plane of Villalobos et al. (2010), Ibsen et al.(2014) and Foglia et al.(2015) are plotted in Figure 8 and compared with the numerical simulations for the same vertical loading. A good agreement is again observed.

### 3.3 Field test

#### 3.3.1 Experimental setup

In order to further validate the numerical model, a reduced scale field test conducted by Houlsby et al. (2005) is simulated hereafter. A steel caisson with an outer diameter of 2m and a skirt length of 2m was tested. The skirt was made of steel plate 12mm thick and the caisson was installed in a shallow pond near the sea to model a bucket foundation. The load eccentricity  $h$  and vertical load  $V$  were 17.4m and 37.3kN, respectively. The caisson was installed in dense Baskarp sand area with unit weight  $19.5\text{kN/m}^3$  and specific gravity  $26.5\text{kN/m}^3$  ( $e_0=0.549$ ) as indicated by (Ibsen et al., 2005). The test contained three phases: installation, loading and dismantling. For the loading phase, an old tower from a wind turbine was mounted on top of the caisson. The caisson was loaded by pulling the tower horizontally with a wire. The combined loading ( $H, M$ ) was controlled by changing the tower height.

#### 3.3.2 Numerical model

The caisson is modelled using rigid hexahedron elements with the same dimensions and thickness as in the experiment (see Figure 9), while the behaviour of the sand is reproduced with the SIMSAND model, see Table 2. The interface behaviour between the caisson and the soil is modelled with a classical Coulomb model, where the tangential frictional stress is assumed proportional to the normal stress. Large deformations and geometric non-linearities are considered. The modelling strategy is similar to that of the indoor model tests (combined Lagrangian - SPH model).

The calculation domain is composed of two parts: the inner SPH domain and the outer Lagrangian domain. The SPH domain has a length of 10m (horizontal direction), a height of

12m and a total number of 106840 particles. The Lagrangian part is discretized with 32670 hexahedral elements. The SPH domain interacts with the Lagrangian finite element domain via contact interfaces that can open and close (ABAQUS, 2014). More specifically and due to the lack of experimental data for the limit stress in the tangential direction, no threshold ( $\tau_{max}$ ) on the tangential frictional stress is adopted. The contact behaviour between the caisson and the soil is modelled by a rigid friction model with a friction coefficient  $\mu = \tan(\phi_c/2) = 0.32$ , where the soil critical friction angle is  $\phi_c = 35.1^\circ$ . A penalty algorithm is adopted for the contact behaviour (Hibbitt et al., 2001). Theoretically, the separation between soil and caisson is allowed. In our cases, the caisson and the soil have not separated during the penetration because of the existence of confining stress and the small thickness of the caisson. The horizontal displacements of the lateral sides are constrained as well as the translational degrees of freedom at the bottom. The different parameters used for the simulation are summarized in Table 2.

### 3.3.3 Caisson foundation simulation results

A moment-rotation test on the 2×2 m caisson is first considered to further prove the robustness of the CLSPH-SIMSAND approach (see Houlsby et al. (2005)). A relatively slow displacement rate of 10 mm/s and a rotation rate of 0.5 degree/s are applied to eliminate dynamic effects. Numerical results are compared with the experimental results in Figure 10. The performance of the model is again satisfactory. The numerical model reproduces correctly not only the moment evolution but also the bearing capacity of the caisson.

An extreme case is shown hereafter to analyse the progressive failure of the field test. The simulation is composed of two steps: the caisson foundation is first installed to the specified depth; then, a displacement rate of 10mm/s and rotation rate of 0.5 degree/s are applied up to the ultimate strength. The plastic deviatoric strain (SDV18), the void ratio (SDV1) and the mean effective stress (S Pressure, kPa) fields are shown in Figure 11 for the

different phases. It is obvious that the area of these three variables increases with increasing applied displacement. The peak value also increases with time. The CLSPH-SIMSAND approach again successfully reproduces the progressive failure of the caisson foundation.

In the following and based on the previous satisfactory validation results, the CLSPH-SIMSAND approach is adopted to numerically reproduce the  $H$ - $M$ - $V$  failure envelope of a caisson foundation for different soil properties and foundation geometries.

## 4 Numerical study of the failure envelope in $H$ - $M$ plane

### 4.1 Loading procedure

In order to identify the failure envelope of a foundation, Gottardi et al. (1999) proposed to follow two loading control paths : (1) *Swipe tests* in which a vertical displacement is first applied to the foundation up to a certain level of vertical force, and then an increasing horizontal displacement under a constant vertical displacement; (2) *Radial displacement tests* in which the ratio between the applied displacements or the combined rotation-displacement increments is kept constant.

In this following, numerical radial displacement tests are adopted as the main loading control. The sign conventions for the loads (horizontal force, vertical force and bending moment) applied on the Loading Reference Point (LRP) of the caisson foundation are presented in Figure 12. The foundation model has an outer diameter ( $D$ ) of 2m, a skirt length ( $L$ ) of 2m, and a lid and skirt thickness ( $t$ ) of 12mm. The main goal of this study being the evaluation of the bearing capacity of the caisson foundation, the wind turbine and the superstructure are not discretised.

OWT caisson foundations are relatively light, with a typical mass of 600t (vertical deadload 6MN) (Houlsby et al., 2005). The horizontal and overturning moment bearing capacities are therefore important for the design. To investigate the form of the failure surface

1 in the  $H$ - $M$  plane, different loading paths are applied hereafter on the LRP of the caisson. As  
2 shown in Figure 13, a constant vertical load is imposed up to a specified value  $\chi = V_i/V_0$  ( $V_0$   
3 being the maximum load). Then, radial displacement loadings are applied considering a  
4 constant ratio between the combined rotation-displacement increments. The value of the  
5 displacement is large enough to ensure that the maximum strength is reached. In the  
6 following  $\chi = 0$  refers to an actual load factor of  $\chi \leq 0.01$  (only the caisson self-weight is  
7 considered).  
8  
9

10 Figure 14 illustrates the way chosen to determine the bearing capacity; the ultimate  
11 bearing capacity is defined by the ends of loading paths. Examples of load paths in the  $H$ - $M$   
12 plane from the numerical radial displacement tests are shown in Figure 15. The ratio between  
13 the increments of the rotation  $\theta$  and the horizontal displacement  $u$  is constant ( $\delta\theta/\delta u \equiv$   
14 constant), which implies a straight loading path (Figure 15(a)). By connecting the values at  
15 the end of the different load paths, the complete failure envelope is obtained, as shown in  
16 Figure 15(b).  
17  
18

19 Note that, to ensure the radial loading paths approaching close enough to the ultimate  
20 capacity diagram, the value of the displacement should be large enough to ensure that the  
21 maximum strength is reached. As shown in Figure 15, the ultimate bearing capacity can be  
22 reached for most of the loading paths, and obvious inflection points can be observed for these  
23 loading cases. However, for a few loading paths, the ultimate bearing capacity is hard to  
24 reach even a large displacement has been occurred. In order to unify the basis of  
25 determination, the ultimate bearing capacity is defined by the ends of loading paths, based on  
26 which the final failure envelope can then be determined.  
27  
28

29 Some general results are summarized below: (1) the failure envelopes of caisson  
30 foundations in sand are of inclined elliptical shape; and (2) the presence of bending moment  
31  
32  
33  
34  
35  
36  
37  
38  
39  
40  
41  
42  
43  
44  
45  
46  
47  
48  
49  
50  
51  
52  
53  
54  
55  
56  
57  
58  
59  
60  
61  
62  
63  
64  
65

has a significant influence on the horizontal bearing capacity depending on the loading direction.

#### 4.2 Influence of the soil properties

The influence of various initial state variables and soil parameters – soil density, friction strength, soil stiffness and grain breakage - on the failure envelope of a caisson foundation in sand is studied hereafter.

Four initial void ratios ( $e_0 = \mathbf{0.62}$ , 0.67, 0.73 and 0.80, corresponding to a relative density  $D_r = 80\%$ , 60%, 40% and 20%), four critical state friction angles ( $\phi_c = 25^\circ$ ,  $30^\circ$ ,  $\mathbf{35.1^\circ}$ ,  $40^\circ$ ), four soil stiffness constants ( $k_p = 0.01$ ,  $\mathbf{0.0034}$ , 0.001, 0.0005; the bigger value represents the smaller stiffness) and four grain breakage constants ( $C_a$  &  $C_b = \mathbf{0 \ \& \ 0}$ , 2500 & 4, 7000 & 7, 12000 & 10) are adopted for the simulations. Note that the set  $e_0 = 0.62$ ,  $\phi_c = 35.1^\circ$ ,  $k_p = 0.0034$ ,  $C_a = 0$  and  $C_b = 0$  corresponds to the Aalborg University Sand No 0 mentioned above. The grain breakage related constants “ $C_a$  &  $C_b = 2500 \ \& \ 4$ , 7000 & 7, 12000 & 10”, corresponds to different crushabilities of a hypothetical sand (Jin et al., 2018). Bold letters are used to represent the original parameter group values corresponding to the field test presented in section 3.3 and Table 2. In order to identify the influence of each property, only one of the related input parameters (including the initial state variable  $e_0$ ) is changed for each numerical simulation while keeping others constant. Three characteristic measures are used to describe the shape and size of the envelope in  $H$ - $M$  space. The length of the long axis  $a$ , the short axis  $b$  and the rotation angle  $\emptyset$ , see Figure 17.

Figure 18 presents the original form and the fitting curve of failure envelopes for varying soil densities in the  $H$ - $M$  plane. It is worth noting that the obtained failure envelope excluded the field case simulated with the original parameter group (marked in bold). For increasing soil density, the size of the failure envelope expands. In other words, the horizontal



and bending moment capacities improve with increasing soil density. A linear relationship can be observed in logarithmic scale between the parameter  $a$  and the soil relative density  $D_r$ , Figure 18(d).

A similar conclusion is obtained regarding the soil friction strength and the stiffness parameters, Figures 19 and 20. With increasing the critical friction angle the mobilized peak strength during shearing is directly increasing, and thus the size of the failure envelope increases. The plastic modulus related constant  $k_p$  is defined as the initial slope of  $q/p'$  versus plastic deviatoric strain. Thus, for a given initial mean effective stress,  $k_p$  controls the initial shear stiffness. In critical-state-based sand models like SIMSAND model adopted in this study, a smaller value of  $k_p$  gives a higher shear modulus resulting in a higher mobilized friction angle or peak strength, as indicated by Yin et al. (2013) and Jin et al. (2016a) that this parameter does not affect the critical strength but influences significantly the peak strength. As a result, in finite element simulations of caisson foundation a smaller value of  $k_p$  representing a higher peak strength of soils gives a bigger size of failure envelope. Or simply speaking, a higher peak strength of foundation soil mobilizes a higher ultimate capacity of caisson foundation. The corresponding asymptotic equations are again linear, implying that the bearing capacity of a caisson foundation improves linearly in logarithmic scale with increasing soil friction strength and soil stiffness.

The horizontal and bending moment bearing capacities decrease when considering grain breakage (see Figure 21). The most significant attenuation occurs for very easily crushable sand (e.g. parameters of Dog's bay sand by Jin et al., 2018). Finally, it should be noted that the short axis  $b$  presents a similar linear trend for different soil properties. On the other hand, the influence of the soil properties on the inclination  $\theta$  of the bearing capacity diagrams is negligible ( $\theta$  remains constant and equal to  $42^\circ$ ).

### 4.3 Influence of the caisson foundation size for the same aspect ratio $L/D$

Previous research works on the failure envelope of caisson foundations mainly focused on model tests on a small scale (Byrne, 2000; Foglia et al., 2015; Houlsby, 2005; Ibsen et al., 2013; Villalobos Jara, 2006). In order to identify the failure envelopes for a full range of caisson sizes, four conventional caisson size aspect ratios ( $L/D = 0.5, 0.75, 1.0, 2.0$ ) are selected for the simulations presented hereafter.  $L$  and  $D$  range from 1m to 20m, details are listed in Table 3. The simulation marked in bold ( $2 \times 2$ m) is the field case simulated in the section 3.3.

The failure envelopes for different caisson sizes  $L/D$  in the  $H$ - $M$  plane are summarized in Figure 22(a)-(c) (the simulation results of the case  $L/D = 0.75$  are presented later on (in the section 4.5). As the variations of the horizontal bearing capacity and the bending moment strength are of the order of four to five, a normalized presentation is adopted in the figures. The main results are: (1) For all conventional caisson sizes  $L/D$  the failure envelopes present a similar inclined elliptical shape. (2) When  $L/D < 1$ , the failure envelopes present a slight tendency to contract with increasing caisson size; for  $L/D = 1$ , the failure envelopes are equivalent. When  $L/D > 1$ , the failure envelopes present a slight tendency to expand. (3) With increasing caisson size  $L/D$ , the failure envelope exhibits a tendency to contract inward; for the same level of bending moment a smaller horizontal bearing capacity is obtained for larger aspect ratios. Yielding (horizontal) or even failure is more likely to occur on a caisson foundation with a larger aspect ratio. On the contrary and for the same level of horizontal force, a greater bending moment strength occurs for large aspect ratio i.e. an offshore wind turbine with a bigger caisson size aspect ratio has a stronger overturning resistance.

Following a similar analysis, the influence of the caisson size characteristics on the failure envelope is presented in Figure 22(d)-(f). Here,  $S$  is the total contact surface area

between the caisson and the soil decomposed in two parts: the surface area of the bottom of the caisson and the surface area of the skirt. The values of the long axis  $a$  for different geometric sizes show a linear increase in logarithmic coordinates; the horizontal bearing capacity and overturning resistance are higher with increasing caisson size. For a specified contact surface area the bearing capacity of the caisson improves slightly with increasing aspect ratio, Figure 22(d). The  $b/a$  ratio ( $b$  the short and  $a$  the long axis) versus the total contact surface area  $S$  is plotted in Figure 22(e). For increasing caisson sizes,  $b/a$  decreases when  $L/D < 1$ , stays constant for  $L/D = 1$  and increases for  $L/D > 1$ . The inclination angle remains however unchanged, Figure 22(f). The influence of the caisson size aspect ratios on the inclination of the bearing capacity diagrams is therefore negligible.

#### 4.4 Influence of the aspect ratio $L/D$ for the same soil-structure contact surface area

A number of studies on caisson foundations were carried out to investigate the influence of the aspect ratio  $L/D$ , experimental (Cassidy et al., 2006; Houlsby et al., 2005; Ibsen et al., 2013; Ibsen et al., 2015; Tran and Kim, 2017; Zhang et al., 2007; Zhu et al., 2014) and numerical (Cassidy et al., 2006; Cheng et al., 2016; Gerolymos et al., 2012; Li et al., 2015; Liu et al., 2014; Zafeirakos and Gerolymos, 2016). In these studies, the  $L$  was changed while  $D$  was kept constant (or vice versa) and therefore the contact surface area was different.

In the following, the impact of the aspect ratio  $L/D$  on the failure envelope is studied for the same soil-structure contact surface area (implying thus the same cost of construction materials). Three groups of aspect ratio combinations are designed with original geometries equal to  $2 \times 2$ m,  $4 \times 4$ m, and  $8 \times 8$ m, details are given in Table 4. The corresponding numerically simulated failure envelopes are shown in Figure 23(a)-(c). Due to the similar sizes, results are not normalized. The main conclusions are: (1) The failure envelopes present different degree inclined elliptical shapes. (2) With increasing  $L/D$  ratio, the failure envelope axis rotates clockwise. During the rotation, the envelope gradually retracts along the short axis and

stretches along the long axis direction. (3) With increasing  $L/D$  ratio, the bearing capacity gradually transforms from horizontal force dominated failure to bending moment failure. For  $L/D < 1$ , the failure envelopes display a horizontal bearing capacity dominated trend; for  $L/D = 1$ , the bearing horizontal force and bending moment capacities are essentially the same; for  $L/D > 1$ , the bending moment bearing capacity is predominant.

During the design phase of caisson foundations for offshore wind turbines an adequate aspect ratio should be therefore selected according to the actual service environment. The relation between the aspect ratio  $L/D$  (for the same soil-structure contact surface area) and the failure envelope is quantified and presented in Figure 23(d)-(f). It can be seen that  $a$  and  $\emptyset$  increase with increasing aspect ratio, while in the contrary the ratio  $b/a$  decreases.

#### 4.5 Combined effect of the soil-structure contact surface and the aspect ratio

In the previous sections, the influence of the caisson foundation size ( $L/D$ ) and the aspect ratio  $L/D$  for the same soil-structure contact surface area on the shape and size of the failure envelope in the  $H-M$  space has been presented in details. A formula is proposed hereafter to describe the coupling effect of the soil-structure contact surface area and the aspect ratio on the failure envelope:

$$\ln(x) = a_1 + a_2 \ln(S) + a_3 \ln(L/D) + a_4 \ln(S) \ln(L/D) \quad (4)$$

where  $x$  represents the failure envelope characteristic measures ( $a$ ,  $b/a$  and  $\emptyset$ );  $S$  is the soil-structure total contact surface area;  $L/D$  is the aspect ratio and  $a_1$ ,  $a_2$ ,  $a_3$  and  $a_4$  are four constants used for fitting. Based on the previous numerical results (sections 4.3 and 4.4), the four constants are calibrated using the Least-Squares Fitting Method in MATLAB. Figure 24 displays the comparison between the numerical and the analytical formula estimated values for the three characteristic measures ( $a$ ,  $b/a$  and  $\emptyset$ ) of the failure envelope. A strong correlation is observed that proves that the proposed formula is applicable for design

purposes and the development of simplified modelling strategies such as the macroelement approach.

## 5 Numerical estimation of the $H$ - $M$ - $V$ failure envelope

### 5.1 Influence of $V_0$ on the $H$ - $M$ failure envelope

The horizontal and overturning moment bearing capacities of caisson foundations vary significantly with the vertical load. In order to quantify this effect, a similar procedure as in section 4 is followed hereafter. More specifically, radial displacement numerical simulation tests are carried out for various levels of vertical load. The failure envelopes for different vertical load levels are presented in Figure 16. The field case shown in Figure 15 is also added ( $\chi = 0.31$ ). It can be concluded that: (1) the influence of the vertical load on the inclination of the bearing capacity diagrams is negligible. (2) the size of the bearing capacity diagram first increases with increasing vertical load and then displays a decreasing trend. This observation agrees with the experimental studies (Villalobos et al., 2009).

### 5.2 Numerical failure envelope in the $H$ - $V$ plane

Numerical radial displacement tests are hereafter performed to identify the failure envelope in the  $H$ - $V$  plane. A displacement vector is applied on the LRP of the caisson foundation (see Figure 13) with an angle varying from 0~180°. The principle of the maximum load (see section 5.1) is again adopted to identify the points of the failure locus, see Figure 25. The obtained failure envelope is similar to the experimental data from Meyerhof (1953), Hansen (1970), DNV (2014) and Ibsen et al. (2014). Due to the high non-linearity the failure points form however an unsmoothed curve. The main results are summarized hereafter: (1) The failure envelopes are symmetric about the  $H/V_0$  axis. (2) A strong interaction is observed between the vertical and the horizontal loads. The horizontal bearing capacity first increases and then decreases. As shown in Figure 25, a peak value is

obtained for a vertical load equal to 0.4~0.5 of the vertical bearing capacity. This agrees with Figure 16 on the  $H-M$  plane. It can be also observed that the horizontal force is non-zero for null vertical loading because of the existence of the skirt.

### 5.3 Numerical failure envelope in the $H-M-V$ 3D space

By combining the results in the  $H-M$  plane for different vertical levels (Figure 15 (b) and Figure 16) and in the  $H-V$  plane (Figure 25), the  $H-M-V$  3D space envelope is plotted in Figure 26. It has inclined elliptical cross-sections along the vertical force axis and its size is controlled by the value of the vertical load.

### 5.4 Influence of the soil properties and the caisson dimensions

The influence of the soil relative density  $D_r$ , the soil stiffness  $k_p$ , the friction angle  $\phi_c$ , the grain breakage and the caisson dimensions (soil-structure contact surface area, aspect ratio) on the vertical bearing capacity  $V_0$  are studied hereafter.

A strong linear tendency can be observed between  $V_0$  and  $D_r$ ,  $\phi_c$  and  $k_p$ , see Figure 27. The vertical bearing capacity decreases for higher sand crushability. The most significant attenuation occurred with the Dog's bay sand, which is the most crushable sand.

The influence of the caisson foundation geometry on  $V_0$  is presented in Table 3 (a similar simulation configuration as in section 4.3 is made). Figure 28 displays the relation between the vertical bearing capacity and the soil-structure contact surface area for three conventional aspect ratios.  $V_0$  and  $S$  present a linear relation in logarithmic coordinates. It is worth noting that for different aspect ratios, the vertical peak-bearing capacity is found the same for similar contact surface areas. In other words, the vertical bearing capacity is mainly controlled by the contact surface area between the soil and the caisson, regardless of the aspect ratio.

To estimate the influence of the aspect ratio, the same soil-structure contact surface is maintained while simultaneously changing the values of  $L$  and  $D$ . The relation between the aspect ratio and the vertical bearing capacity for three geometry levels is shown in Figure 29.  $V_0$  and  $L/D$  present a linear negative correlation in logarithmic coordinates; for the same surface contact area a bigger  $L/D$  implies smaller contact area between the bottom of the caisson and the soil. Furthermore, for the same aspect ratio the vertical bearing capacity increases with an increase in the caisson's geometry because of the contact area increase at the bottom of the caisson.

The same analytical equation as in section 4.5 is adopted to describe the coupling between geometry, aspect ratio and vertical bearing capacity. Figure 30 illustrates the comparison between the simulation-based values and the formula-estimated values for a given vertical bearing capacity. The proposed analytical formula successfully reproduces the simulation results.

As presented and discussed above, a large number of simulations were carried out to investigate the behaviour of a caisson foundation subjected to different load combinations in this study. The average computation time for each case approximately equals to 8 hours by adopting eight cores (processor clock speed equals to 2.50 GHz). Note that several cases can be submitted and calculated simultaneously owing to the *LIGER* server and related computation resources provided by ECN (Ecole Centrale de Nantes, France), the method and number of simulations are acceptable.

## 6 Analytical equations for the failure envelope

## 6.1 Analytical equations for the failure envelope in the $H$ - $M$ plane

As shown in Section 4.1, the failure envelope in the  $H$ - $M$  plane has an inclined elliptical shape. Following Villalobos et al. (2009), a similar formula is introduced to reproduce the inclined failure envelope of a caisson foundation in sand:

$$y = \left( \frac{H}{h_i V_0} \right)^2 + \left( \frac{M}{Dm_i V_0} \right)^2 + 2e \frac{H}{h_i V_0} \frac{M}{Dm_i V_0} - 1 = 0 \quad (5)$$

The general shape of the surface is determined by the parameters  $h_i$ ,  $m_i$ , and  $e$ . The fitting parameters  $h_i$  and  $m_i$  represent the intersection of each ellipse with the  $H/V_0$  and  $M/DV_0$  axes respectively,  $e$  being the eccentricity of each ellipse. Using this equation, the yield points simulated in the previous sections can be fitted using a least-squares regression.

Eq. (5) satisfies the implicit equation of an ellipse, also referred to as the general equation:

$$A_1 X^2 + A_2 XY + A_3 Y^2 + A_4 X + A_5 Y + A_6 = 0 \quad (6)$$

The general equation's coefficients can be obtained from the semi-major axis  $a$ , the semi-minor axis  $b$ , the centre coordinates  $(x_c, y_c)$  and the rotation angle  $\phi$  of the failure envelope using the following formulae:

$$\begin{cases} A_1 = a^2 (\sin \phi)^2 + b^2 (\cos \phi)^2 \\ A_2 = 2(b^2 - a^2) \sin \phi \cos \phi \\ A_3 = a^2 (\cos \phi)^2 + b^2 (\sin \phi)^2 \\ A_4 = -2A_1 x_c - A_2 y_c \\ A_5 = -A_2 x_c - 2A_3 y_c \\ A_6 = A_1 x_c^2 + A_2 x_c y_c + A_3 y_c^2 - a^2 b^2 \end{cases} \quad (7)$$

The centre coordinates of the failure envelope in the  $H$ - $M$  plane coincide with the origin.  $A_4$ ,  $A_5$  and  $A_6$  therefore become:



$$\begin{cases} A_4 = 0 \\ A_5 = 0 \\ A_6 = -a^2 b^2 \end{cases} \quad (8)$$

Here, only three parameters,  $a$ ,  $b$  and  $\phi$  describe the shape and size of the failure envelope in the  $H$ - $M$  plane. By comparing Eq. (5) and Eq. (6),  $h_i$ ,  $m_i$  and  $e$  are expressed as follows:

$$\begin{cases} h_i = \frac{ab}{V_0 \sqrt{a^2 \sin^2 \phi + b^2 \cos^2 \phi}} \\ m_i = \frac{ab}{V_0 \sqrt{a^2 \cos^2 \phi + b^2 \sin^2 \phi}} \\ e = \frac{\sin \phi \cos \phi (a^2 - b^2)}{\sqrt{(a^2 \sin^2 \phi + b^2 \cos^2 \phi)(a^2 \cos^2 \phi + b^2 \sin^2 \phi)}} \end{cases} \quad (9)$$

It must be pointed out that the values of  $a$  and  $b$  are related to the current vertical loading level  $\chi$ . The coupling relationships among the characteristic measures of the failure envelope, soil-structure contact surface area and aspect ratio have been comprehensively analysed and quantified through Eq. (4). For a given caisson geometry, the failure envelope in the  $H$ - $M$  space for a given soil can be therefore obtained using Eq. (4), Eq. (5) and Eq. (9).

Using Eq. (9), the fitted parameters  $h_i$ ,  $m_i$  and  $e$  of the first group of aspect ratio combinations studied in section 4.4 are displayed in Table 5, in which the original geometry (field test) equals 2×2m. Figure 31 shows the comparison of Eq. (5) with the numerical results for the normalized failure envelope in the  $H$ - $M$  plane. It is observed that the proposed equation fits well the different yield points.

## 6.2 Analytical equations for the failure envelope in the $H$ - $M$ - $V$ 3D space

Figure 32 shows how  $h_i$  and  $m_i$  vary with the normalized load  $V/V_0$ . It can be seen that the apex of the yield surface at low vertical loads is not at the origin but at a negative value

because of the tension capacity of the caisson foundation. The tension capacity needs to be considered in order to obtain a more reasonable expression for the 3D yield surface.

The proposed formula is similar to that proposed by Villalobos et al. (2009) but in a more concise form.

$$h_i = \frac{H_i}{V_0} = h_0 \left( \frac{\beta_1^{\beta_1} + \beta_2^{\beta_2}}{t_0 + 1} \right)^{\left( \frac{\beta_1 + \beta_2}{\beta_1 \beta_2} \right)} \left( \frac{V}{V_0} + t_0 \right)^{\beta_1} \left( 1 - \frac{V}{V_0} \right)^{\beta_2} \quad (10)$$

$$m_i = \frac{M_i}{V_0} = m_0 \left( \frac{\beta_1^{\beta_1} + \beta_2^{\beta_2}}{t_0 + 1} \right)^{\left( \frac{\beta_1 + \beta_2}{\beta_1 \beta_2} \right)} \left( \frac{V}{V_0} + t_0 \right)^{\beta_1} \left( 1 - \frac{V}{V_0} \right)^{\beta_2} \quad (11)$$

The two parameters  $\beta_1$  and  $\beta_2$  are shaping parameters that allow to best fit the data and are generally close to unity (larger values will make the failure envelope concave (Ibsen et al., 2013)).  $h_0$  and  $m_0$  are the maximum values of  $h_i$  and  $m_i$  over the full range of  $V/V_0$ .  $t_0$  controls the tension loading that the caisson foundation can sustain. It can be obtained by using a function of the skirt thickness  $t$  relative to the diameter of the caisson (Villalobos et al. 2004, 2005).

Eq. (5), (10) and (11) can be combined to represent an inclined parabolic ellipsoid in the 3D  $H$ - $M$ - $V$  plane as follows:

$$y = \left( \frac{H}{h_0 V_0} \right)^2 + \left( \frac{M}{D m_0 V_0} \right)^2 + 2e \frac{H}{h_0 V_0} \frac{M}{D m_0 V_0} - F(V, V_t, V_0) = 0 \quad (12)$$

Where

$$F(V, V_t, V_0) = \beta_{12}^2 \left( \frac{V}{V_0} + t_0 \right)^{2\beta_1} \left( 1 - \frac{V}{V_0} \right)^{2\beta_2}, \beta_{12} = \left( \frac{\beta_1^{\beta_1} + \beta_2^{\beta_2}}{t_0 + 1} \right)^{\left( \frac{\beta_1 + \beta_2}{\beta_1 \beta_2} \right)} \quad (13)$$

Here  $V_t$  is the tension capacity of the caisson foundation. An example of the complete three-dimensional shape of the rotated yield surface is shown in Figure 33.

The parameters obtained from the best curve fitting with the numerical results are presented in Table 6. The 3D failure envelope for a caisson foundation in sand according to Eq. (12) is plotted in Figure 34(a). The expressions proposed by Gottardi et al. (1999), Byrne and Houlsby (1999) and Villalobos et al. (2009) are also plotted in Figures 34(b), 34(c) and 34(d). The correlation factor  $R^2$  is estimated as 0.88, 0.67, 0.79 and 0.82, respectively indicating that Eq. (12) is more suitable to reproduce the 3D failure envelope of the caisson foundation.

## 7 Conclusions

A numerical study combining the Lagrangian-SPH method (CLSPH) and the elastoplasticity constitutive law SIMSAND is presented to identify the failure envelope of caisson foundation in sand. The soil parameters of the SIMSAND model were first calibrated from a series of triaxial tests on Baskarp sand. A simulation of a cone penetration test was then conducted to validate the CLSPH-SIMSAND modelling strategy. A series of model tests and a field test of a caisson foundation were also selected and simulated. Results demonstrated that the CLSPH-SIMSAND approach was able to reproduce the response of caisson foundation in sand with the calibrated soil parameters.

Then, a large number of finite element numerical calculations were carried out to investigate the behaviour of a caisson foundation subjected to different load combinations. The radial displacement method was adopted for the simulations. A series of factors including the soil density, friction strength, soil stiffness, grain crushability, the caisson geometry and aspect ratio, were considered to study the failure envelope. Finally, an analytical formula was proposed to describe the 3D failure envelope in the  $H$ - $M$ - $V$  space that

can be used for the design and the development of simplified modelling strategies as the macroelement approach.

## Acknowledgements

This research was financially supported by a RIF project (Grant No.: PolyU R5037-18F) and a GRF project (Grant No.: 15209119) from Research Grants Council (RGC) of Hong Kong Special Administrative Region Government (HKSARG) of China, and the National Natural Science Foundation of China (Grant No. 51579179).

## Reference

- ABAQUS, I., 2014. Abaqus documentation. Version 6, 5-1.
- Achmus, M., Akdag, C.T., Thieken, K., 2013. Load-bearing behavior of suction bucket foundations in sand. *Applied Ocean Research* 43, 157-165.
- Bojanowski, C., 2014. Numerical modeling of large deformations in soil structure interaction problems using FE, EFG, SPH, and MM-ALE formulations. *Archive of applied mechanics* 84, 743-755.
- Byrne, B., Houlsby, G., 1999. Drained behaviour of suction caisson foundations on very dense sand, *Offshore Technology Conference*. Offshore Technology Conference. Houston, paper 10994.
- Byrne, B., Houlsby, G., 2001. Observations of footing behaviour on loose carbonate sands. *Géotechnique* 51 (5), 463-466.
- Byrne, B.W., 2000. Investigations of suction caissons in dense sand. University of Oxford Oxford, UK.
- Cassidy, M., Byrne, B., Houlsby, G., 2002. Modelling the behaviour of circular footings under combined loading on loose carbonate sand. *Géotechnique* 52 (10), 705-712.
- Cassidy, M., Randolph, M., Byrne, B., 2006. A plasticity model describing caisson behaviour in clay. *Applied Ocean Research* 28 (5), 345-358.
- Chen, W., Qiu, T., 2012. Numerical Simulations for Large Deformation of Granular Materials Using Smoothed Particle Hydrodynamics Method. *International Journal of Geomechanics* 12, 127-135.
- Cheng, X., Wang, J., Wang, Z., 2016. Incremental elastoplastic FEM for simulating the deformation process of suction caissons subjected to cyclic loads in soft clays. *Applied Ocean Research* 59, 274-285.

- Cremer, C., Pecker, A., Davenne, L., 2001. Cyclic macro - element for soil - structure interaction: material and geometrical non - linearities. *International journal for numerical and analytical methods in geomechanics* 25 (13), 1257-1284.
- DNV, D.N.V., 2013. Design of offshore wind turbine structures. Standard DNV-OSJ101, Det Norske Veritas AS (DNV).
- ABAQUS, I., 2014. Abaqus documentation. Version 6, 5-1. Dassault Systèmes Simulia Corp., Providence, RI, USA.
- Foglia, A., Gottardi, G., Govoni, L., Ibsen, L.B., 2015. Modelling the drained response of bucket foundations for offshore wind turbines under general monotonic and cyclic loading. *Applied Ocean Research* 52, 80-91.
- Gerolymos, N., Zafeirakos, A., Karapiperis, K., 2015. Generalized failure envelope for caisson foundations in cohesive soil: static and dynamic loading. *Soil Dynamics and Earthquake Engineering* 78, 154-174.
- Gerolymos, N., Zafeirakos, A., Souliotis, C., 2012. Insight to failure mechanisms of caisson foundations under combined loading: A macro-element approach, *Proc. 2nd Int. Conf. on Performance-based design in Earthquake Geotechnical Engineering*, Taormina, Italy.
- Gingold, R.A., Monaghan, J.J., 1977. Smoothed particle hydrodynamics: theory and application to non-spherical stars. *Monthly notices of the royal astronomical society* 181 (3), 375-389.
- Gottardi, G., Butterfield, R., 1993. On the bearing capacity of surface footings on sand under general planar loads. *Soils and foundations* 33 (3), 68-79.
- Gottardi, G., Houlsby, G., Butterfield, R., 1999. Plastic response of circular footings on sand under general planar loading. *Géotechnique* 49 (4), 453-470.
- Gourvenec, S., Barnett, S., 2011. Undrained failure envelope for skirted foundations under general loading. *Géotechnique* 61 (3), 263-270.
- Gourvenec, S., Randolph, M., 2003. Effect of strength non-homogeneity on the shape of failure envelopes for combined loading of strip and circular foundations on clay. *Géotechnique* 53 (6), 575-586.
- Grange, S., Kotronis, P., Mazars, J., 2008. A macro - element for a circular foundation to simulate 3D soil - structure interaction. *International journal for numerical and analytical methods in geomechanics* 32 (10), 1205-1227.
- Hansen, J.B., 1970. A revised and extended formula for bearing capacity. *Danish Geotechnical Institute, Bulletin No. 28*, 5-11.
- Hibbitt, Karlsson, Sorensen, 2001. ABAQUS/Explicit: User's Manual. Hibbitt, Karlsson and Sorenson Incorporated.
- Hogervorst, J.R., 1980. Field trials with large diameter suction piles, *Offshore Technology Conference*. Offshore Technology Conference.
- Houlsby, G., 2005. The theoretical modelling of circular shallow foundation for offshore wind turbines. *University of Oxford*.
- Houlsby, G., Cassidy, M., 2002. A plasticity model for the behaviour of footings on sand under combined loading. *Géotechnique* 52 (2), 117-129.

- Houlsby, G.T., Ibsen, L.B., Byrne, B.W., 2005. Suction caissons for wind turbines. *Frontiers in Offshore Geotechnics: ISFOG*, Perth, WA, Australia, 75-93.
- Houlsby, G.T., Kelly, R.B., Huxtable, J., Byrne, B.W., 2006. Field trials of suction caissons in sand for offshore wind turbine foundations. *Géotechnique* 56, 3-10.
- Ibsen, L.B., Barari, A., Larsen, K.A., 2013. Adaptive plasticity model for bucket foundations. *Journal of engineering mechanics* 140 (2), 361-373.
- Ibsen, L.B., Barari, A., Larsen, K.A., 2015. Effect of Embedment on the Plastic Behavior of Bucket Foundations. *Journal of Waterway, Port, Coastal & Ocean Engineering* 141, 1-9.
- Ibsen, L.B., Larsen, K.a., Barari, a., 2014. Calibration of Failure Criteria for Bucket Foundations on Drained Sand under General Loading. *Journal of geotechnical and geoenvironmental engineering* 140, 04014033.
- Ibsen, L.B., Liingaard, S., Nielsen, S.A., 2005. Bucket Foundation, a status. *Proceedings of the Copenhagen Offshore Wind*. 26-28 October, Copenhagen, Denmark.
- Iskander, M., El-Gharbawy, S., Olson, R., 2002. Performance of suction caissons in sand and clay. *Canadian Geotechnical Journal* 39, 576-584.
- Jin, Y.-F., Wu, Z.-X., Yin, Z.-Y., Shen, J.S., 2017. Estimation of critical state-related formula in advanced constitutive modeling of granular material. *Acta Geotechnica*, 1-23.
- Jin, Y.-F., Yin, Z.-Y., Shen, S.-L., Hicher, P.-Y., 2016a. Investigation into MOGA for identifying parameters of a critical-state-based sand model and parameters correlation by factor analysis. *Acta Geotechnica* 11 (5), 1131-1145.
- Jin, Y.-F., Yin, Z.-Y., Shen, S.-L., Hicher, P.-Y., 2016b. Selection of sand models and identification of parameters using an enhanced genetic algorithm. *International journal for numerical and analytical methods in geomechanics* 40, 1219-1240.
- Jin, Y.-F., Yin, Z.-Y., Wu, Z.-X., Daouadji, A., 2018a. Numerical modeling of pile penetration in silica sands considering the effect of grain breakage. *Finite Elements in Analysis and Design* 144, 15-29.
- Jin, Z., Yin, Z.-Y., Kotronis, P., Jin, Y.-F., 2018b. Numerical investigation on evolving failure of caisson foundation in sand using the combined Lagrangian-SPH method. *Marine Georesources & Geotechnology*, 1-13.
- Li, D., Zhang, Y., Feng, L., Gao, Y., 2015. Capacity of modified suction caissons in marine sand under static horizontal loading. *Ocean Engineering* 102, 1-16.
- Li, S., Liu, W.K., 2002. Meshfree and particle methods and their applications. *Applied Mechanics Reviews* 55 (1), 1-34.
- Li, Z., Kotronis, P., Escoffier, S., 2014. Numerical study of the 3D failure envelope of a single pile in sand. *Computers and Geotechnics* 62.
- Li, Z., Kotronis, P., Escoffier, S., Tamagnini, C., 2016. A hypoplastic macroelement for single vertical piles in sand subject to three-dimensional loading conditions. *Acta Geotechnica* 11 (2), 373-390.
- Liu, M., Yang, M., Wang, H., 2014. Bearing behavior of wide-shallow bucket foundation for offshore wind turbines in drained silty sand. *Ocean Engineering* 82, 169-179.
- Meyerhof, G.t., 1953. The bearing capacity of foundations under eccentric and inclined loads, *Proc. of the 3rd Int. Conf. on SMFE*, pp. 440-445.

- Montrasio, L., Nova, R., 1997. Settlements of shallow foundations on sand: geometrical effects. *Géotechnique* 47 (1), 49-60.
- Nguyen-Sy, L., 2005. The theoretical modelling of circular shallow foundation for offshore wind turbines. University of Oxford.
- Nguyen-Sy, L., Houlsby, G.T., 2005. The theoretical modelling of a suction caisson foundation using hyperplasticity theory. *Frontiers in Offshore Geotechnics II*, Perth, 417.
- Nova, R., Montrasio, L., 1991. Settlements of shallow foundations on sand. *Géotechnique* 41 (2), 243-256.
- Ortiz, M., Simo, J., 1986. An analysis of a new class of integration algorithms for elastoplastic constitutive relations. *International Journal for Numerical Methods in Engineering* 23 (3), 353-366.
- Salciarini, D., Tamagnini, C., 2009. A hypoplastic macroelement model for shallow foundations under monotonic and cyclic loads. *Acta Geotechnica* 4 (3), 163-176.
- Senders, M., 2009. Suction caissons in sand as tripod foundations for offshore wind turbines. University of Western Australia.
- Sheng, D., Sloan, S., Yu, H., 2000. Aspects of finite element implementation of critical state models. *Computational mechanics* 26 (2), 185-196.
- Skau, K.S., Grimstad, G., Page, A.M., Eiksund, G.R., Jostad, H.P., 2018. A macro-element for integrated time domain analyses representing bucket foundations for offshore wind turbines. *Marine Structures* 59, 158-178.
- Tjelta, T.I., 1995. Geotechnical experience from the installation of the Europipe jacket with bucket foundations, Offshore Technology Conference. Offshore Technology Conference. Houston, Paper OTC 7795.
- Tjelta, T.I., 2001. Suction piles: their position and application today, The Eleventh International Offshore and Polar Engineering Conference. International Society of Offshore and Polar Engineers. Stavanger, Vol. 2, 1-6.
- Tran, N.X., Kim, S.-R., 2017. Evaluation of horizontal and moment bearing capacities of tripod bucket foundations in sand. *Ocean Engineering* 140, 209-221.
- Villalobos, F., Byrne, B., Houlsby, G., Martin, C., 2003. Bearing capacity tests of scale suction caisson footings on sand: Experimental data. Data Rep. FOT005/1, Dept. of Engineering Science, Univ. of Oxford, Oxford, UK.
- Villalobos, F.A., Byrne, B.W., Houlsby, G.T., 2005. Moment loading of caissons installed in saturated sand, Proceedings of international symposium on frontiers in Geotechnics, ISFOG. University of Western, pp. 411-416.
- Villalobos, F.A., Byrne, B.W., Houlsby, G.T., 2009. An experimental study of the drained capacity of suction caisson foundations under monotonic loading for offshore applications. *Soils and foundations* 49 (3), 477-488.
- Villalobos, F.A., Byrne, B.W., Houlsby, G.T., 2010. Model testing of suction caissons in clay subjected to vertical loading. *Applied Ocean Research* 32 (4), 414-424.
- Villalobos, F.A., Houlsby, G.T., Byrne, B.W., 2004. Suction caisson foundations for offshore wind turbines, Proc. 5th Chilean Conference of Geotechnics (Congreso Chileno de Geotecnia), Santiago, pp. 24-26.

- Villalobos Jara, F.A., 2006. Model testing of foundations for offshore wind turbines. University of Oxford.
- Wu, Z.-X., Yin, Z.-Y., Jin, Y.-F., Geng, X.-Y., 2017. A straightforward procedure of parameters determination for sand: a bridge from critical state based constitutive modelling to finite element analysis. *European Journal of Environmental and Civil Engineering*, 1-23.
- Yao, Y., Hou, W., Zhou, A., 2009. UH model: three-dimensional unified hardening model for overconsolidated clays. *geotechnique* 59 (5), 451-469.
- Yao, Y., Lu, D., Zhou, A., Zou, B., 2004. Generalized non-linear strength theory and transformed stress space. *Science in China Series E: Technological Sciences* 47 (6), 691-709.
- Yao, Y., Sun, D., Matsuoka, H., 2008. A unified constitutive model for both clay and sand with hardening parameter independent on stress path. *Computers and Geotechnics* 35 (2), 210-222.
- Yin, Z.-Y., Chang, C.S., Hicher, P.-Y., 2010. Micromechanical modelling for effect of inherent anisotropy on cyclic behaviour of sand. *International Journal of Solids and Structures* 47 (14-15), 1933-1951.
- Yin, Z.-Y., Xu, Q., Hicher, P.-Y., 2013. A simple critical state based double-yield-surface model for clay behavior under complex loading. *Acta Geotechnica* 8(5): 509-523.
- Yin, Z.-Y., Hicher, P.-Y., Dano, C., Jin, Y.-F., 2017a. Modeling Mechanical Behavior of Very Coarse Granular Materials. *Journal of engineering mechanics* 143, C4016006.
- Yin, Z.-Y., Jin, Y.-F., Shen, S.-L., Huang, H.-W., 2017b. An efficient optimization method for identifying parameters of soft structured clay by an enhanced genetic algorithm and elastic-viscoplastic model. *Acta Geotechnica* 12, 849-867.
- Yin, Z.-Y., Jin, Z., Kotronis, P., Wu, Z.-X., 2018. Novel SPH SIMSAND-Based Approach for Modeling of Granular Collapse. *International Journal of Geomechanics* 18 (11), 04018156.
- Yin, Z.Y., Chang, C.S., 2013. Stress-dilatancy behavior for sand under loading and unloading conditions. *International journal for numerical and analytical methods in geomechanics* 37 (8), 855-870.
- Zafeirakos, A., Gerolymos, N., 2016. Bearing strength surface for bridge caisson foundations in frictional soil under combined loading. *Acta Geotechnica* 11 (5), 1189-1208.
- Zhang, J.H., Zhang, L.M., Lu, X.B., 2007. Centrifuge modeling of suction bucket foundations for platforms under ice-sheet-induced cyclic lateral loadings. *Ocean Engineering* 34, 1069-1079.
- Zhu, B., Zhang, W.-l., Ying, P.-p., Chen, Y.-m., 2014. Deflection-Based Bearing Capacity of Suction Caisson Foundations of Offshore Wind Turbines. *Journal of geotechnical and geoenvironmental engineering* 140, 1-12.



# Table

Table 1 Basic constitutive equations of the SIMSAND model

| Components                                | Constitutive equations   |
|---|--|
| Elasticity                                | $\dot{\varepsilon}_{ij}^e = \frac{1+\nu}{3K(1-2\nu)} \sigma'_{ij} - \frac{\nu}{3K(1-2\nu)} \sigma'_{kk} \delta_{ij}$ $K = K_0 \cdot p_{at} \frac{(2.97-e)^2}{(1+e)} \left( \frac{p'}{p_{at}} \right)^\zeta$  |
| Yield surface                             | $f = \frac{q}{p'} - H$   |
| Potential surface                         | $\frac{\partial g}{\partial p'} = A_d \left( M_{pt} - \frac{q}{p'} \right); \quad \frac{\partial g}{\partial s_{ij}} = \{1 \quad 1 \quad 1 \quad 1 \quad 1 \quad 1\}$  |
| Hardening rule                            | $H = \frac{M_p \varepsilon_d^p}{k_p + \varepsilon_d^p}$  |
| Critical state with inter-locking effects | $e_c = e_{ref} - \lambda \left( \frac{p'}{p_{at}} \right)^\xi \quad \tan \phi_p = \left( \frac{e_c}{e} \right)^{n_p} \quad \tan \phi_{pt} = \left( \frac{e_c}{e} \right)^{-n_d} \tan \phi_\mu$   |
| Three-dimensional strength criterion      | $M_p = \frac{6 \sin \phi_p}{3 - \sin \phi_p} \left[ \frac{2c_1^4}{1 + c_1^4 + (1 - c_1^4) \sin 3\theta} \right]^{\frac{1}{4}} \quad \text{with } c_1 = \frac{3 - \sin \phi_p}{3 + \sin \phi_p}$ $M_{pt} = \frac{6 \sin \phi_{pt}}{3 - \sin \phi_{pt}} \left[ \frac{2c_2^4}{1 + c_2^4 + (1 - c_2^4) \sin 3\theta} \right]^{\frac{1}{4}} \quad \text{with } c_2 = \frac{3 - \sin \phi_{pt}}{3 + \sin \phi_{pt}}$ |
| Grain breakage related equations          | $e_{ref} = e_{refu} + (e_{ref0} - e_{refu}) \exp(-C_b B_r^*)$ $B_r^* = \frac{w_p}{C_a + w_p} \quad \text{with } w_p = \int (p' \langle d \varepsilon_v^{pl} \rangle + q d \varepsilon_d^{pl})$   |

\*  $p_{at}$  is the atmospheric pressure ( $p_{at} = 101.3$  kPa);  $p'$  is the effective mean pressure;  $q$  is the deviatoric stress;  $e_c$  is the critical state void ratio;  $\phi_p$  is the peak friction angle;  $\phi_{pt}$  the phase transformation friction angle;  $M_{pt}$  is the stress ratio corresponding to the phase transformation;  $M_p$  is the peak stress ratio;  $\theta$  is the Lode's angle with its effect introduced as in Sheng et al. (2000) and Yao et al. (2004, 2008 and 2009);  $n_p$  and  $n_d$  are parameters controlling the degree of interlocking due to neighboring particles, Yin and Chang (2010, 2013);  $e_{refu}$  is the ultimate initial critical void ratio corresponding to virgin soil without grain breakage and fractal crushed soil ( $=e_{min}$  in this study for simplicity);  $C_b$  is a material constant which controls the decreasing rate of the Critical State Line (CSL) due to grain breakage;  $C_a$  is a material constant controlling the evolution rate of the modified grain breakage index, Jin et al. (2018a).

Table 2 Calibrated parameters of the SIMSAND model for the Baskarp sand

| Parameters       | Name   | Value  |
|------------------|--|--------|
| $K_0$            | Referential bulk modulus (dimensionless)             | 344    |
| $\nu$            | Poisson's ratio                                      | 0.25   |
| $n$              | Elastic constant controlling the nonlinear stiffness | 0.58   |
| $\phi_c$         | Critical state friction angle                        | 35.1   |
| $e_{\text{ref}}$ | Initial critical state void ratio                    | 1.25   |
| $\lambda$        | First constant controlling the nonlinearity of CSL   | 0.38   |
| $\xi$            | Second constant controlling the nonlinearity of CSL  | 0.11   |
| $A_d$            | Constant of magnitude of the stress-dilatancy        | 0.45   |
| $k_p$            | Plastic modulus related constant                     | 0.0034 |

Table 3 Geometry size configurations

| $L/D = 0.5$ | $L/D = 0.75$ | $L/D = 1.0$ | $L/D = 2.0$ |
|-------------|--------------|-------------|-------------|
| 1×2m        | 1.5×2m       | <b>2×2m</b> | 2×1m        |
| 2×4m        | 3×4m         | 4×4m        | 4×2m        |
| 4×8m        | 6×8m         | 8×8m        | 8×4m        |
| 8×16m       | 12×16m       | 16×16m      | 16×8m       |
| 10×20m      | 15×20m       | 20×20m      | 20×10m      |

Table 4 Geometry size configurations for a constant surface contact area

| $S = 15.7 \text{ m}^2$ |          |          | $S = 62.8 \text{ m}^2$ |          |          | $S = 251.3 \text{ m}^2$ |          |          |
|------------------------|----------|----------|------------------------|----------|----------|-------------------------|----------|----------|
| $L$ (m)                | $D$ (m)  | $L/D$    | $L$ (m)                | $D$ (m)  | $L/D$    | $L$ (m)                 | $D$ (m)  | $L/D$    |
| 1                      | 2.83     | 0.35     | 2                      | 5.8      | 0.34     | 4                       | 11.6     | 0.34     |
| 1.5                    | 2.31     | 0.65     | <b>4</b>               | <b>4</b> | <b>1</b> | 6                       | 9.55     | 0.63     |
| <b>2</b>               | <b>2</b> | <b>1</b> | 6                      | 2.97     | 2.02     | <b>8</b>                | <b>8</b> | <b>1</b> |
| 3.56                   | 1.5      | 2.37     | 8                      | 2.33     | 3.43     | 12                      | 5.94     | 2.02     |
| 4.15                   | 1.39     | 3        | 10                     | 1.91     | 5.23     | 20                      | 3.82     | 5.23     |

Table 5 Intersection and eccentricity parameters:  $h_i$ ,  $m_i$  and  $e$ 

| $L$ (m) | $D$ (m) | $L/D$ | $V/V_0$ | $a$   | $b$  | $\phi$ (°) | $h_i$  | $m_i$  | $e$   |
|---------|---------|-------|---------|-------|------|------------|--------|--------|-------|
| 1       | 2.83    | 0.35  | 0.18    | 4793  | 1820 | 25.4       | 0.1005 | 0.0601 | 0.657 |
| 1.5     | 2.31    | 0.65  | 0.26    | 5655  | 1518 | 36.4       | 0.1054 | 0.0808 | 0.871 |
| 2       | 2       | 1     | 0.31    | 6155  | 1308 | 42.1       | 0.0982 | 0.0896 | 0.913 |
| 3.56    | 1.5     | 2.37  | 0.26    | 15855 | 1557 | 63.9       | 0.0760 | 0.1521 | 0.970 |
| 4.15    | 1.39    | 3     | 0.28    | 21546 | 1878 | 66.3       | 0.0962 | 0.2151 | 0.973 |

Table 6 Parameters of the proposed failure surface for the 2×2 m caisson foundation

| Parameter | Name                                    | Value |
|-----------|---|-------|
| $V_0$     | Vertical bearing capacity: kN           | 19330 |
| $t_0$     | Tension factor                          | 0.06  |
| $e$       | Eccentricity of yield surface           | 0.913 |
| $h_0$     | Dimension of yield surface (horizontal) | 0.145 |
| $m_0$     | Dimension of yield surface (moment)     | 0.138 |
| $\beta_1$ | Shaping factor of yield surface         | 0.99  |
| $\beta_2$ | Shaping factor of yield surface         | 0.95  |

## Figure captions

Figure 1 Calibration of SIMSAND model parameters from isotropic compression test on Baskarp sand

Figure 2 Calibration of the SIMSAND model parameters from drained triaxial tests on Baskarp sand with void ratios varying from 0.61 to 0.85 and stress levels from 5 to 800 kPa: (a-c) ratio of deviatoric stress to mean effective stress ( $q/p'$ ) versus axial strain; (d) void ratio versus mean effective stress in semi-logarithmic scale; (e) void ratio versus axial strain

Figure 3 Combined Lagrangian-SPH model for the indoor model tests: (a) 3D mesh, and (b) middle cross section

Figure 4 Results of the CPT test: (a) combined Lagrangian-SPH model, (b) comparison of  $q$ - $w$  curves between experiments and simulation, fields of (c,f,i) plastic deviatoric strain, (d,g,j) void ratio, (e,h,k) mean effective stress during penetration

Figure 5 Results of the pure vertical penetration test: (a) comparison of vertical force - vertical displacement between experiment and simulation, fields of (b) plastic deviatoric strain, (c) void ratio and (d) mean effective stress at the end of the vertical penetration test

Figure 6 Comparison between simulated and experimental results for indoor model tests of a caisson foundation under combined loadings: (a)  $H$  versus  $U$ , and (b)  $M/D$  versus  $D\theta$

Figure 7 Simulated progressive failure of the  $M/DH=3.01$  test; peak values and post-peak values: fields of (a,d) plastic deviatoric strain, (b,e) void ratio, (c,f) mean effective stress

Figure 8 Comparison between simulated and experimental results; failure envelopes on the  $H:M/D$  loading plane

Figure 9 Combined Lagrangian-SPH model for the field test: (a) 3D mesh, and (b) middle cross section

Figure 10 Comparison between simulated results and field measurements: moment  $M$  and rotation  $D\theta$  curve

Figure 11 Simulated results of the field test at different phases: (a) end of penetration, (b)  $\frac{1}{2}$  of the peak values of the forces, (c) peak values of the forces, and (d) post-failure stage

Figure 12 Loading and displacement conventions for a caisson foundation

Figure 13 Schematic plot of radial displacement control

Figure 14 Determination of failure points according to end states of loading paths based on curves of (a) moment  $M$  versus Horizontal force  $H$ , (b) Horizontal force  $H$  versus displacement  $u$ , and (c) moment  $M$  versus rotation  $\theta$

Figure 15 Numerical results of radial displacement control tests in the  $H$ - $M$  plane: (a) load paths, and (b) failure surface

Figure 16 Failure envelopes at different vertical load levels in the  $H$ - $M$  plane

Figure 17 Schematic plot of the failure envelope and definitions of the characteristic measures  $a$ ,  $b$  and  $\emptyset$

Figure 18 Failure envelopes in the  $H$ - $M$  plane for different relative sand densities: (a)  $D_r = 20\%$ , (b)  $D_r = 40\%$ , (c)  $D_r = 60\%$ , and (d) correlation between the ellipse size  $a$  and  $D_r$

Figure 19 Failure envelopes in the  $H$ - $M$  plane for different sand critical friction angles: (a)  $\phi_c = 25^\circ$ , (b)  $\phi_c = 30^\circ$ , (c)  $\phi_c = 40^\circ$ , and (d) correlation between the ellipse size  $a$  and  $\phi_c$

Figure 20 Failure envelopes in the  $H$ - $M$  plane for different soil stiffnesses: (a)  $K_p = 0.01$ , (b)  $K_p = 0.001$ , (c)  $K_p = 0.0005$ , and (d) correlation between the ellipse size  $a$  and  $K_p$

Figure 21 Failure envelopes in the  $H$ - $M$  plane for different sand grain crushabilities: (a) easy crushing, (b) medium crushing, (c) hard crushing, and (d) ellipse size  $a$  versus crushability

Figure 22 Normalized failure envelopes in the  $H$ - $M$  plane for different geometry sizes: (a)  $L/D = 0.5$ , (b)  $L/D = 1.0$ , (c)  $L/D = 2.0$  and plot of the failure envelope characteristic measures versus the contact surface area  $S$  (d) ellipse size  $a$ , (e) ratio  $b/a$ , and (f) inclination angle  $\emptyset$

Figure 23 Failure envelopes in the  $H$ - $M$  plane for different geometry sizes: (a)  $2 \times 2$ m, (b)  $4 \times 4$ m, (c)  $8 \times 8$ m, and plot of the failure envelope characteristic measures versus the aspect ratio  $L/D$ : (d) ellipse size  $a$ , (e) ratio  $b/a$ , and (f) inclination angle  $\emptyset$

Figure 24 Comparison between numerically obtained characteristic measures and formula estimated values for: (a) size of ellipse  $a$  (b) 3D plot of  $a$  versus  $S$  and  $L/D$ , (c)  $b/a$  with (d) 3D plot of  $b/a$  versus  $S$  and  $L/D$ , and (e) inclination angle  $\emptyset$  with (f) 3D plot of  $\emptyset$  versus  $S$  and  $L/D$

Figure 25 Numerical results for various load paths and approximate failure envelope in  $H$ - $V$  plane

Figure 26 Failure envelope in the three-dimensional  $H$ - $M$ - $V$  space (numerical simulations)

Figure 27 Relationship between vertical bearing capacity  $V_0$  and related soil properties: (a) relative density, (b) critical friction angle, (c) plastic stiffness and (d) sand grain crushability

Figure 28 Vertical bearing capacity  $V_0$  versus contact surface area  $S$  for different aspect ratios  $L/D$

Figure 29 Vertical bearing capacity  $V_0$  versus aspect ratio  $L/D$

Figure 30 (a) Comparison between the vertical bearing capacity  $V_0$  and the formula estimated  $V_0$ , and (b) 3D plot of the correlation between  $V_0$ , the contact surface area  $S$  and the aspect ratio  $L/D$

Figure 31 Comparison of fitted curves by the analytical equation and numerical results for different aspect ratios: (a)  $L/D=0.35, 0.65$  and  $1$ , (b)  $L/D=2.37$  and  $3$

Figure 32 Intersection points  $h_i$  and  $m_i$  as a function of the normalized vertical load  $V/V_0$

Figure 33 Illustration of the yield surface shaped as a parabola and inclined ellipse in the  $(V, M/D, H)$  load space

Figure 34 Numerical yield points fitted by the three-dimensional failure envelopes based on (a) Eq. (12), (b) Gottardi et al. (1999), (c) Byrne and Houlsby (1999) and (d) Villalobos et al. (2009)

## Figure

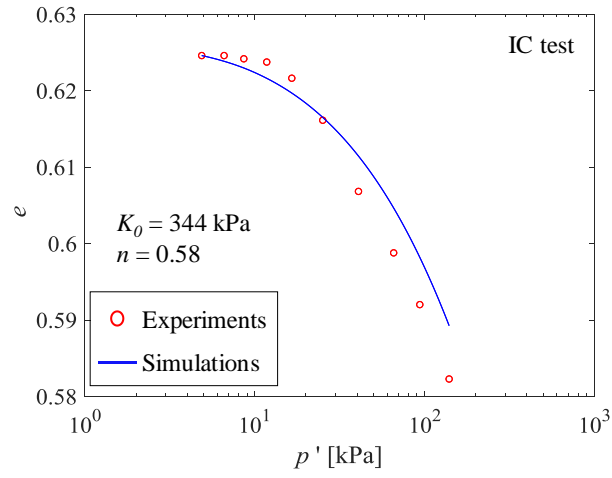


Figure 1 Calibration of SIMSAND model parameters from isotropic compression test on Baskarp sand

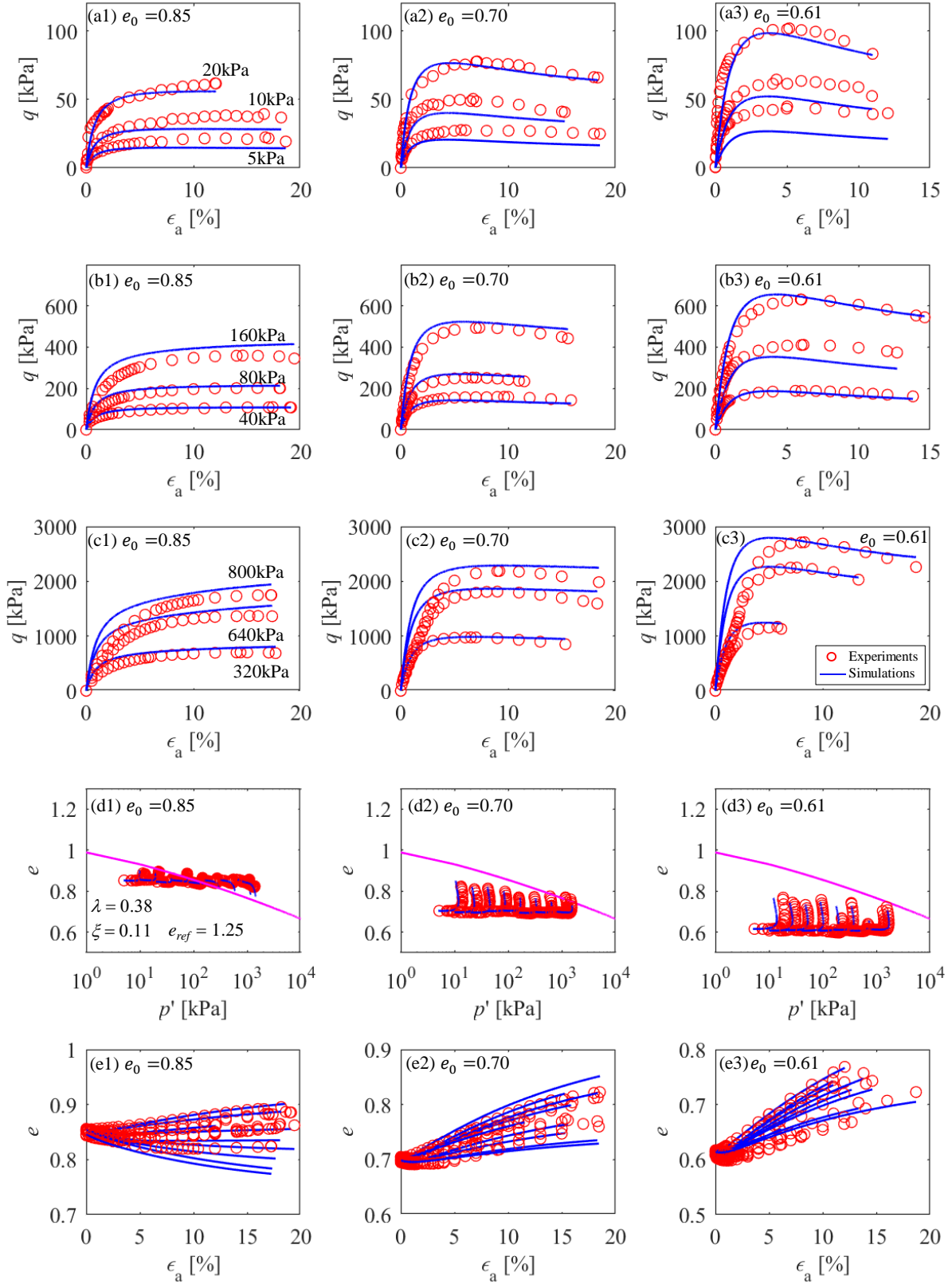


Figure 2 Calibration of the SIMSAND model parameters from drained triaxial tests on Baskarp sand with void ratios varying from 0.61 to 0.85 and stress levels from 5 to 800 kPa: (a-c) ratio of deviatoric stress to mean effective stress ( $q/p'$ ) versus axial strain; (d) void ratio versus mean effective stress in semi-logarithmic scale; (e) void ratio versus axial strain



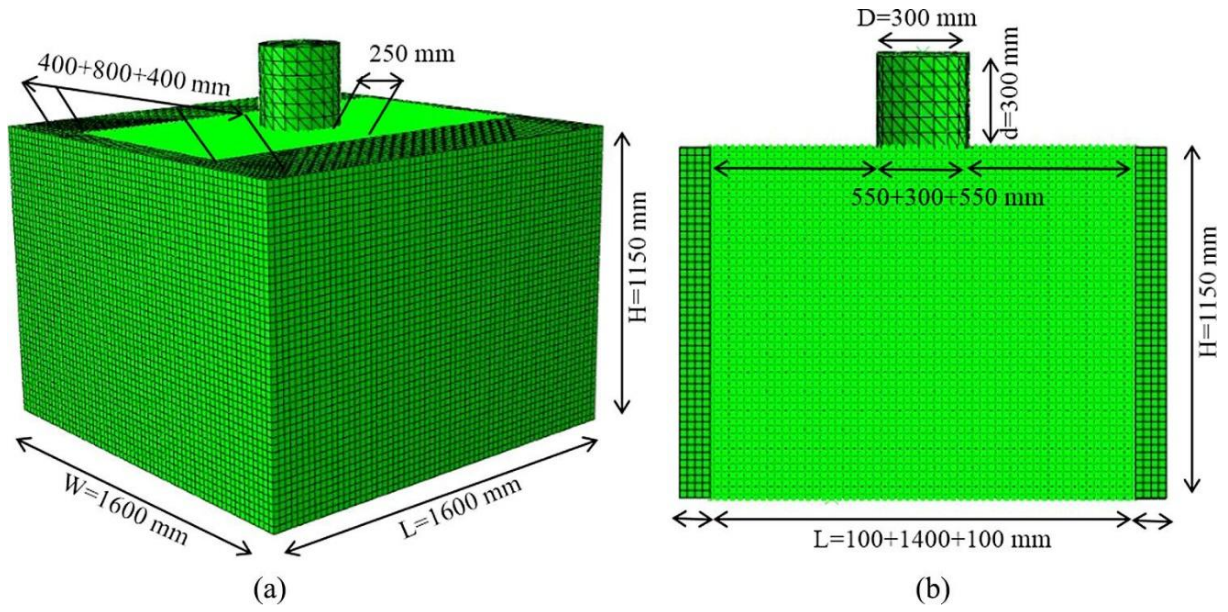
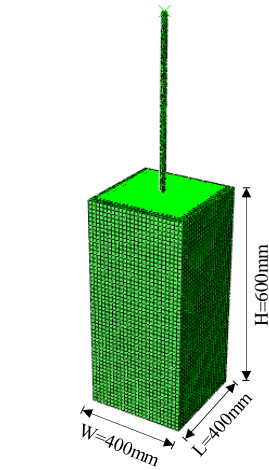
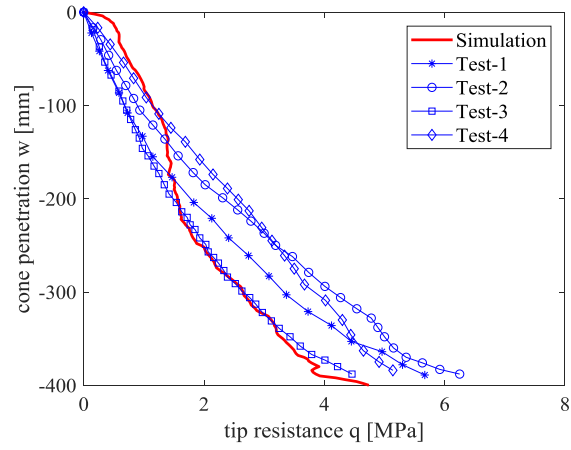


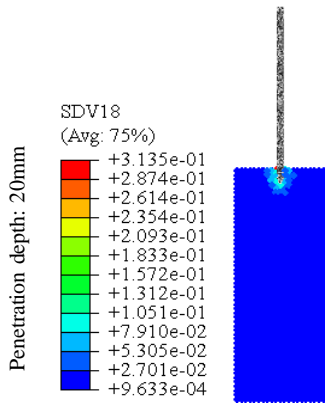
Figure 3 Combined Lagrangian-SPH model for the indoor model tests: (a) 3D mesh, and (b) middle cross section



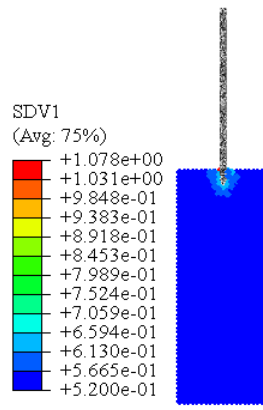
(a) combined Lagrangian-SPH model



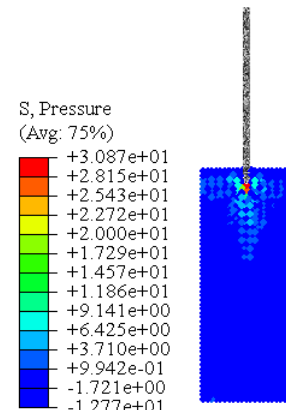
(b) comparison of q-w curves between experiments and simulation



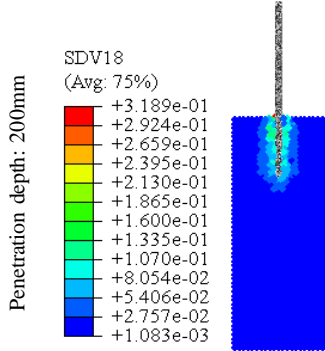
(c) Plastic deviatoric strain



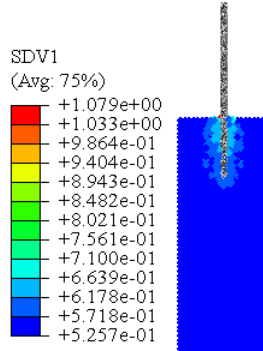
(d) Void ratio



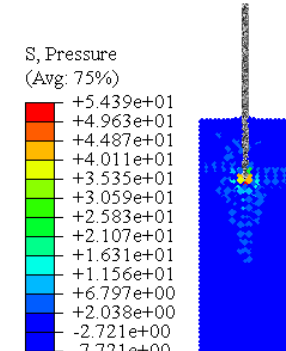
(e) Mean effective stress



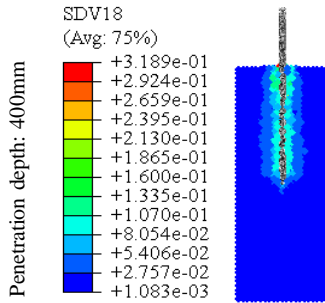
(f) Plastic deviatoric strain



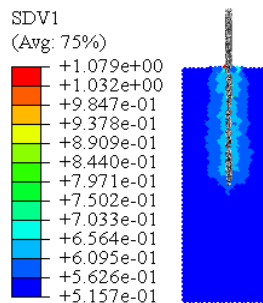
(g) Void ratio



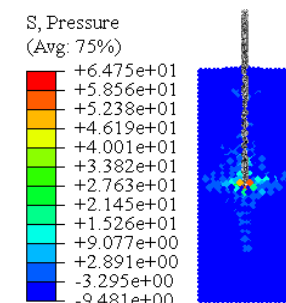
(h) Mean effective stress



(i) Plastic deviatoric strain



(j) Void ratio



(k) Mean effective stress

Figure 4 Results of the CPT test: (a) combined Lagrangian-SPH model, (b) comparison of q-w curves between experiments and simulation, fields of (c,f,i) plastic deviatoric strain, (d,g,j) void ratio, (e,h,k) mean effective stress during penetration

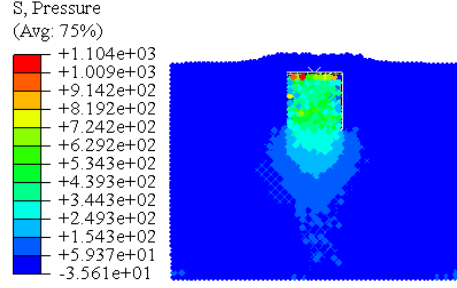
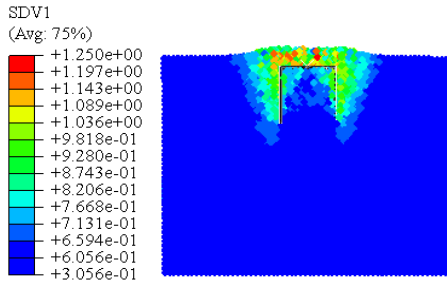
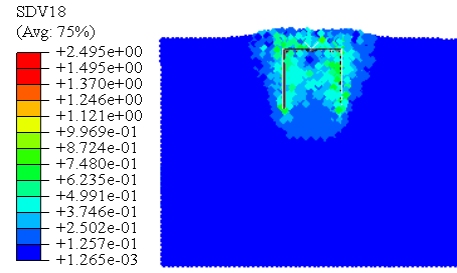
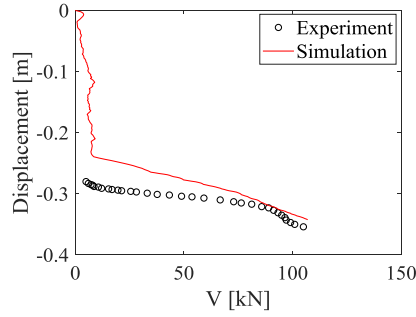


Figure 5 Results of the pure vertical penetration test: (a) comparison of vertical force - vertical displacement between experiment and simulation, fields of (b) plastic deviatoric strain, (c) void ratio and (d) mean effective stress at the end of the vertical penetration test

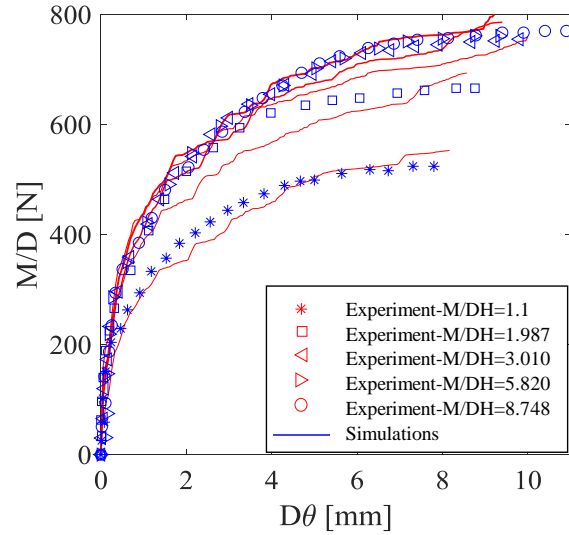
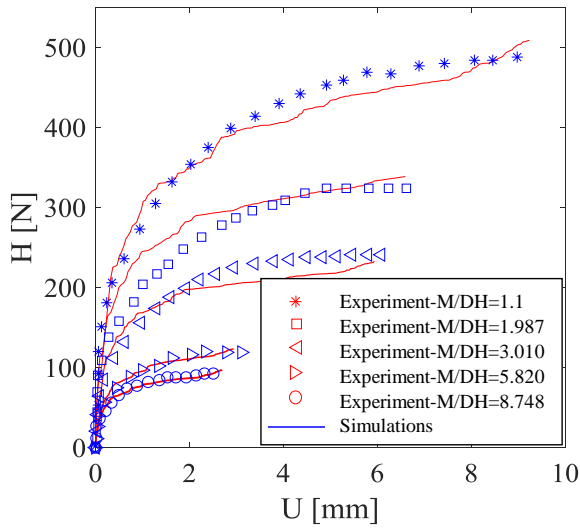


Figure 6 Comparison between simulated and experimental results for indoor model tests of a caisson foundation under combined loadings: (a) H versus U, and (b) M/D versus  $D\theta$

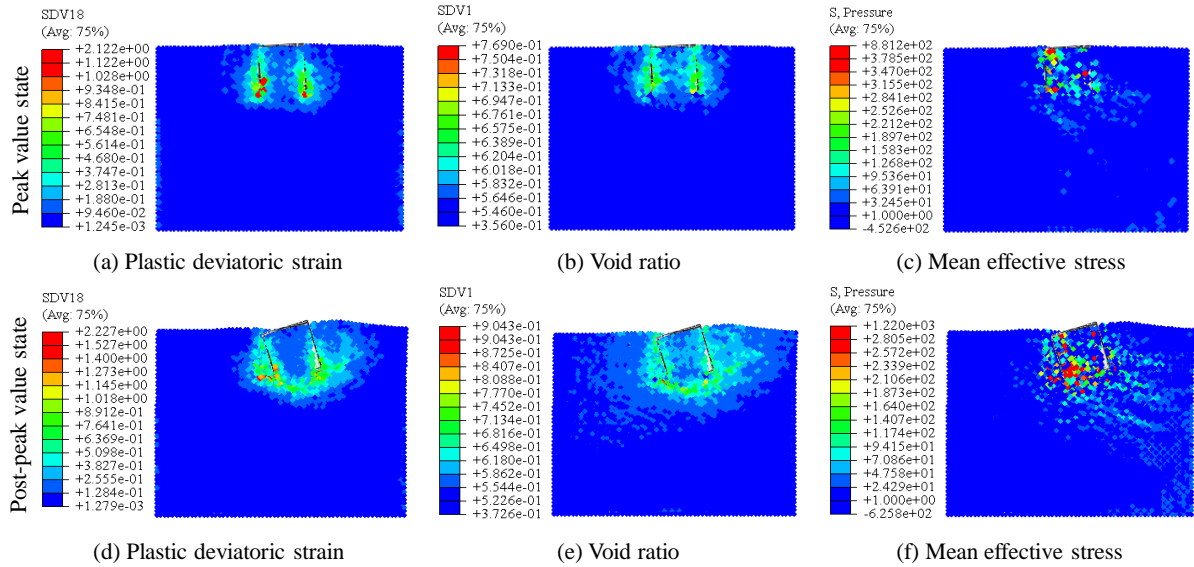


Figure 7 Simulated progressive failure of the  $M/DH=3.01$  test; peak values and post-peak values: fields of (a,d) plastic deviatoric strain, (b,e) void ratio, (c,f) mean effective stress

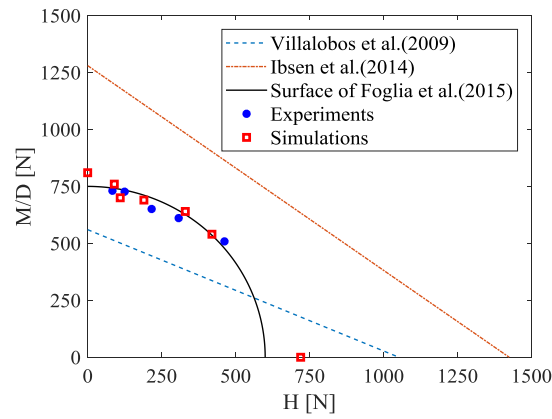


Figure 8 Comparison between simulated and experimental results; failure envelopes on the  $H:M/D$  loading plane

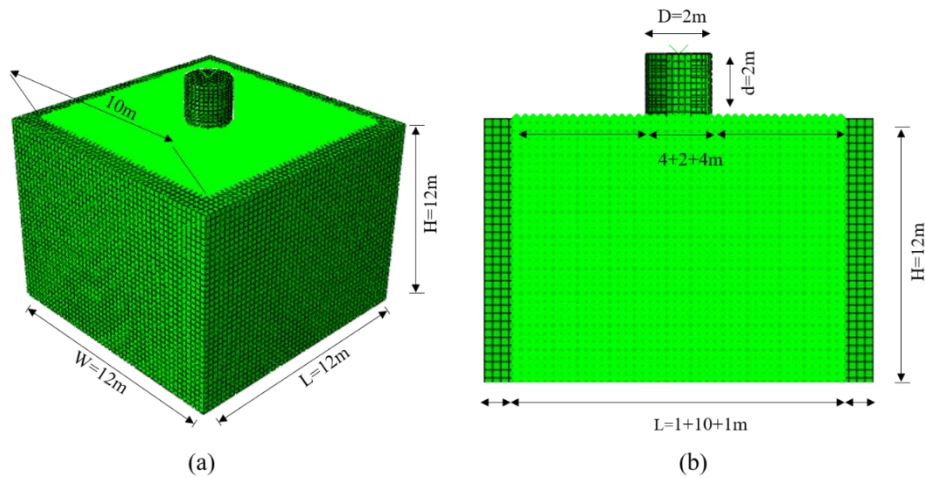


Figure 9 Combined Lagrangian-SPH model for the field test: (a) 3D mesh, and (b) middle cross section

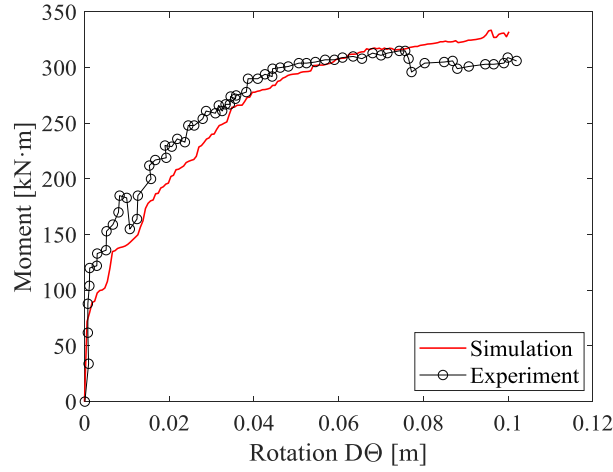


Figure 10 Comparison between simulated results and field measurements: moment  $M$  and rotation  $D\theta$  curve

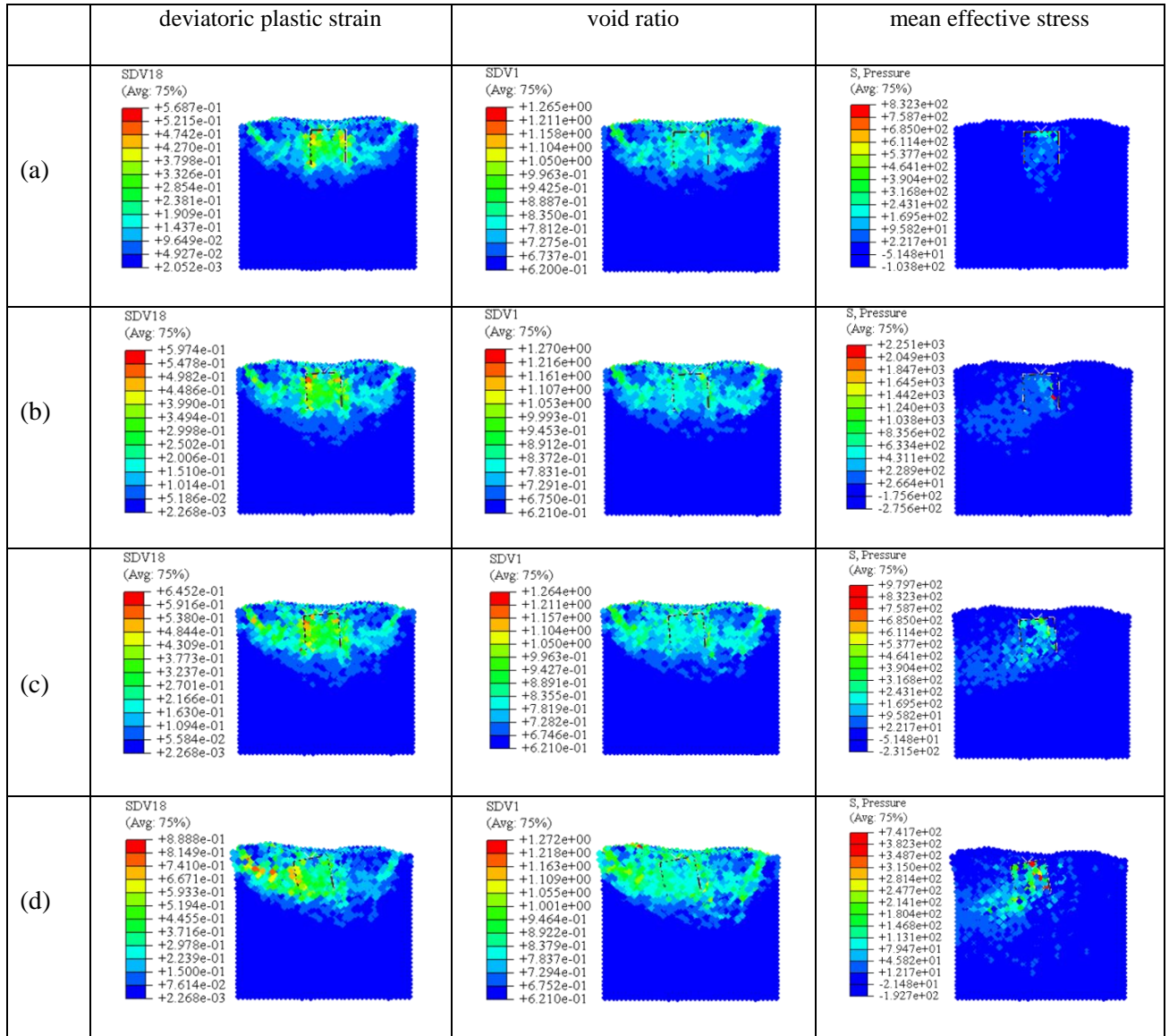


Figure 11 Simulated results of the field test at different phases: (a) end of penetration, (b)  $\frac{1}{2}$  of the peak values of the forces, (c) peak values of the forces, and (d) post-failure stage

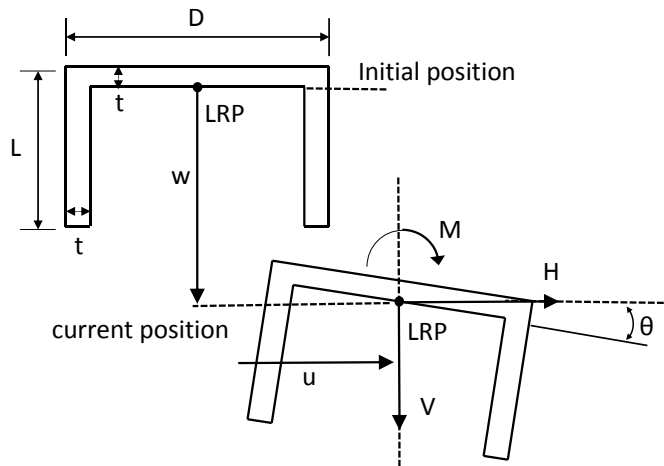


Figure 12 Loading and displacement conventions for a caisson foundation

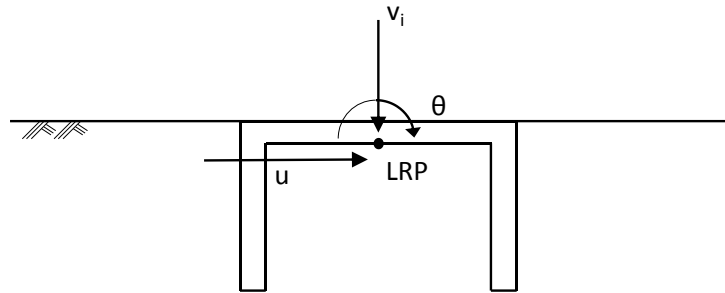


Figure 13 Schematic plot of radial displacement control



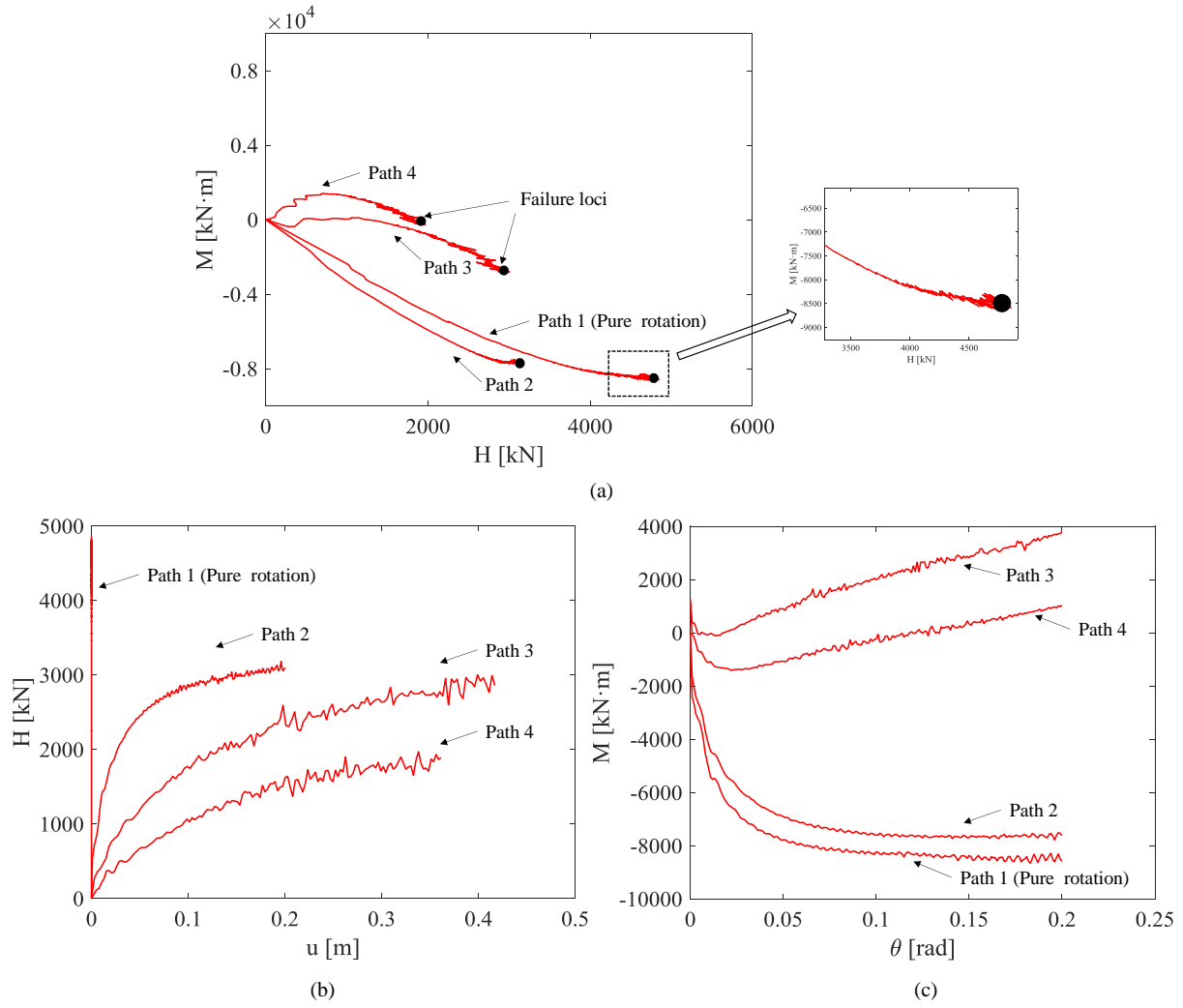


Figure 14 Determination of failure points according to end states of loading paths based on curves of (a) moment  $M$  versus Horizontal force  $H$ , (b) Horizontal force  $H$  versus displacement  $u$ , and (c) moment  $M$  versus rotation  $\theta$

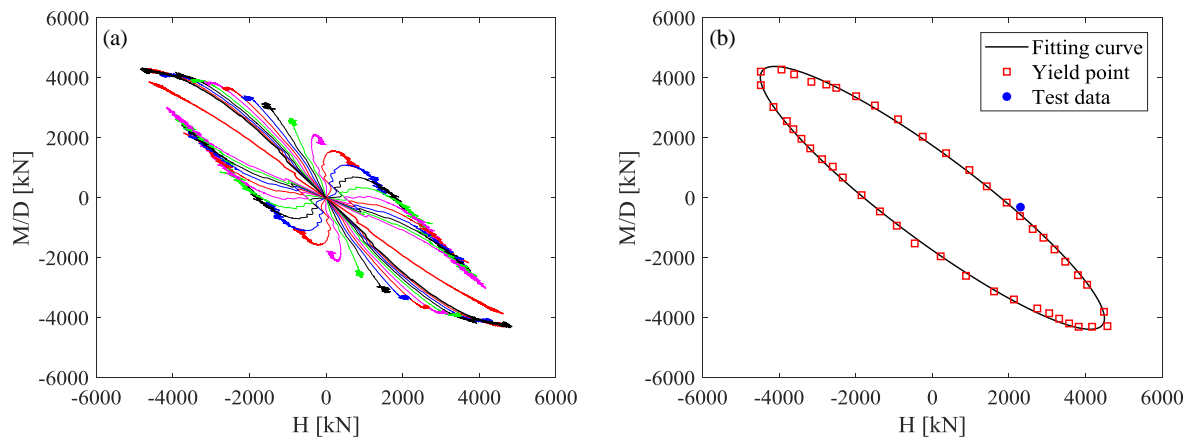


Figure 15 Numerical results of radial displacement control tests in the  $H$ - $M$  plane: (a) load paths, and (b) failure surface

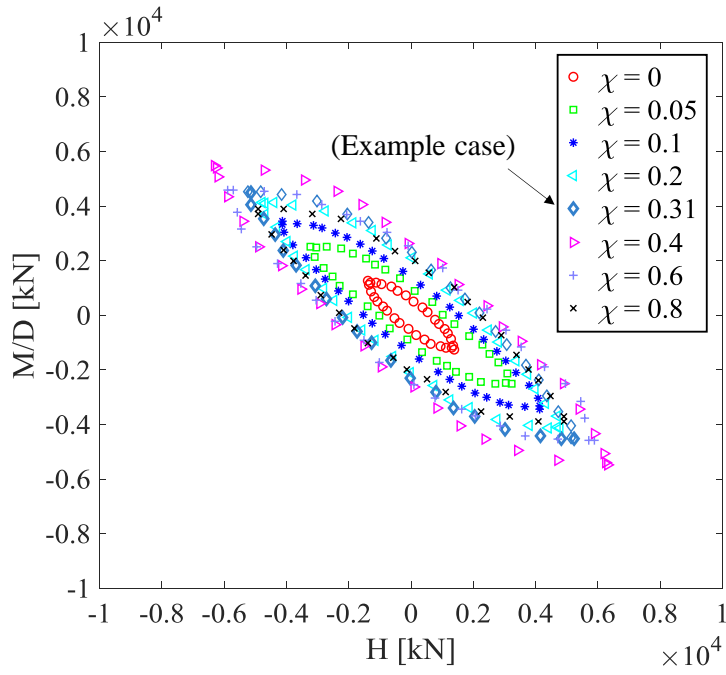


Figure 16 Failure envelopes at different vertical load levels in the  $H$ - $M$  plane

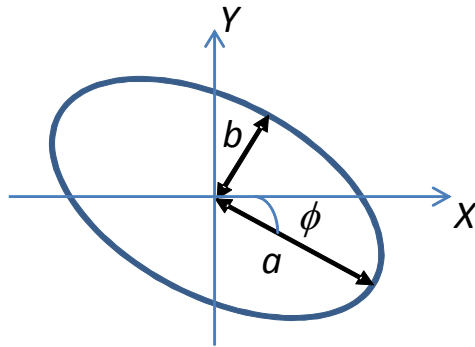


Figure 17 Schematic plot of the failure envelope and definitions of the characteristic measures  $a$ ,  $b$  and  $\phi$



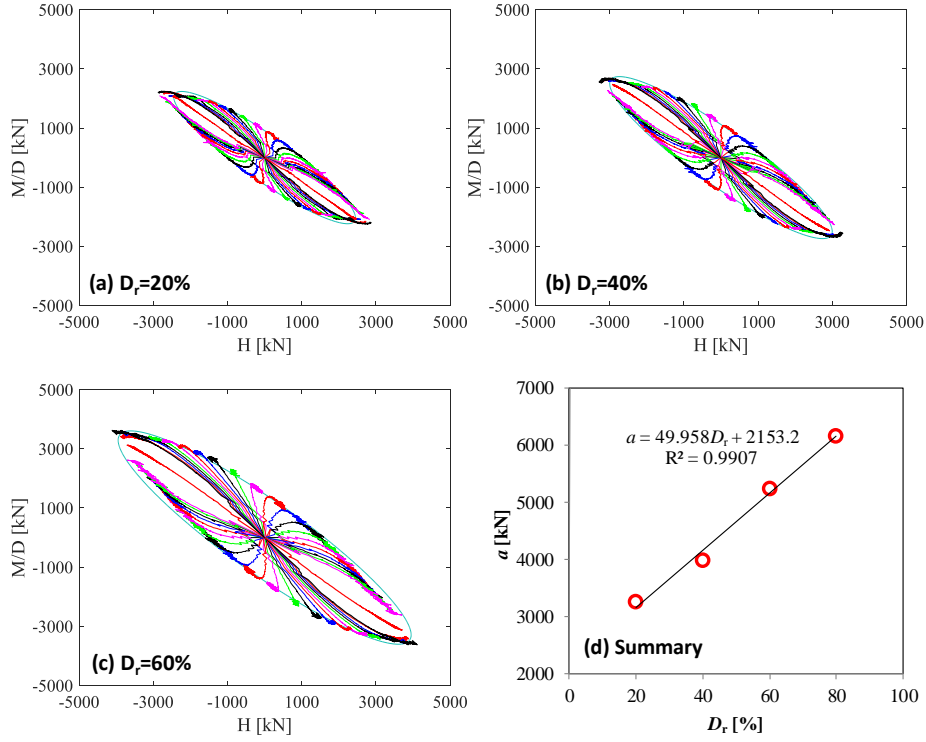


Figure 18 Failure envelopes in the  $H$ - $M$  plane for different relative sand densities: (a)  $D_r = 20\%$ , (b)  $D_r = 40\%$ , (c)  $D_r = 60\%$ , and (d) correlation between the ellipse size  $a$  and  $D_r$

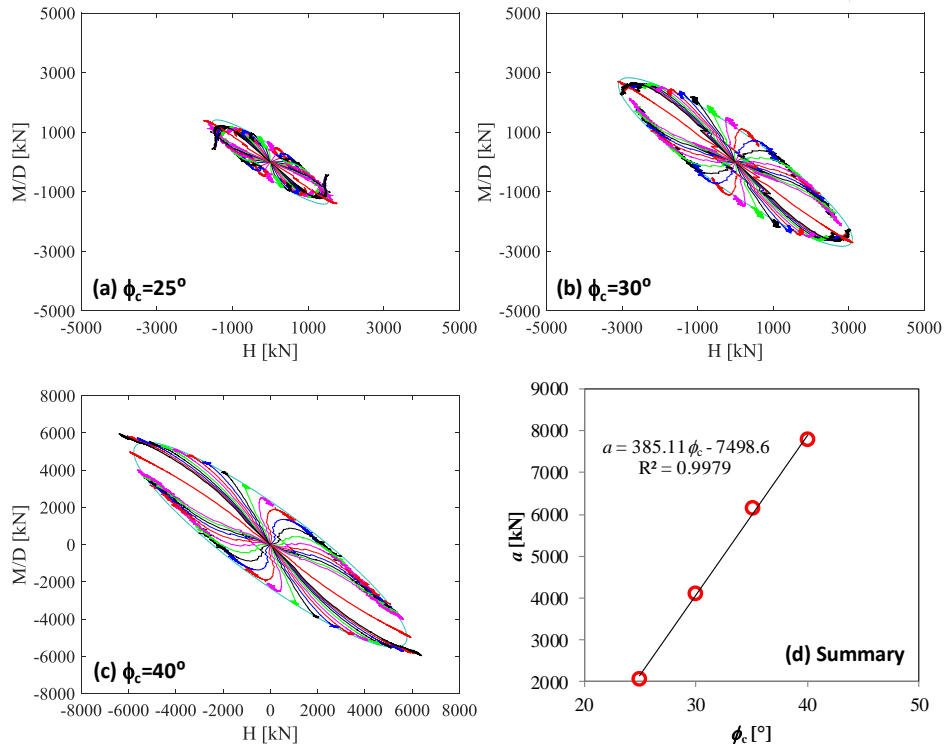


Figure 19 Failure envelopes in the  $H$ - $M$  plane for different sand critical friction angles: (a)  $\phi_c = 25^\circ$ , (b)  $\phi_c = 30^\circ$ , (c)  $\phi_c = 40^\circ$ , and (d) correlation between the ellipse size  $a$  and  $\phi_c$

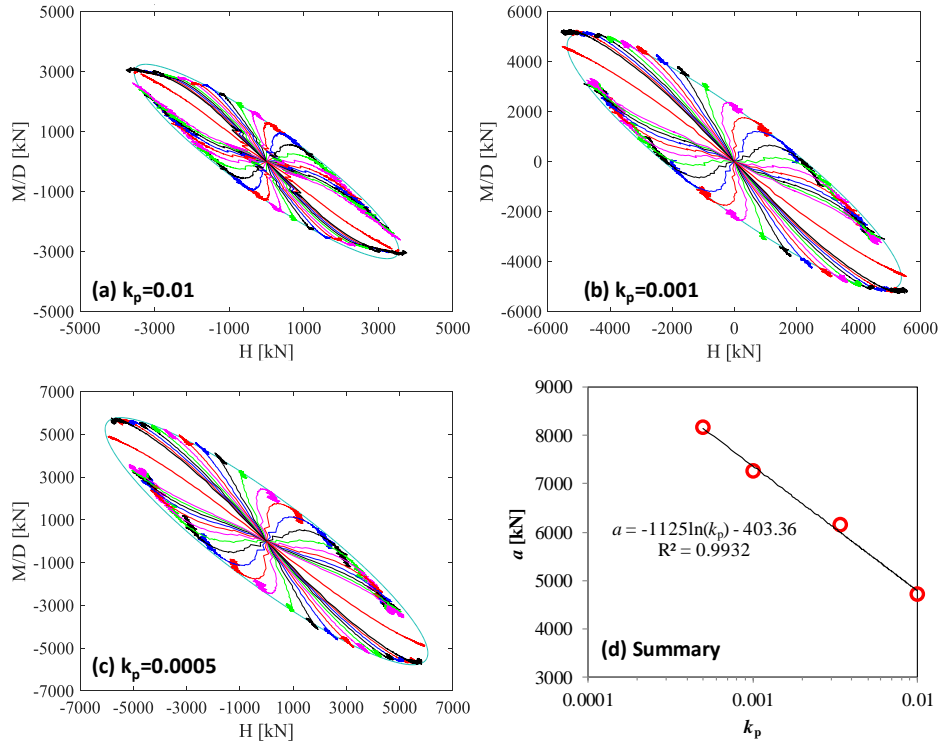


Figure 20 Failure envelopes in the H-M plane for different soil stiffnesses: (a)  $K_p = 0.01$ , (b)  $K_p = 0.001$ , (c)  $K_p = 0.0005$ , and (d) correlation between the ellipse size  $a$  and  $K_p$

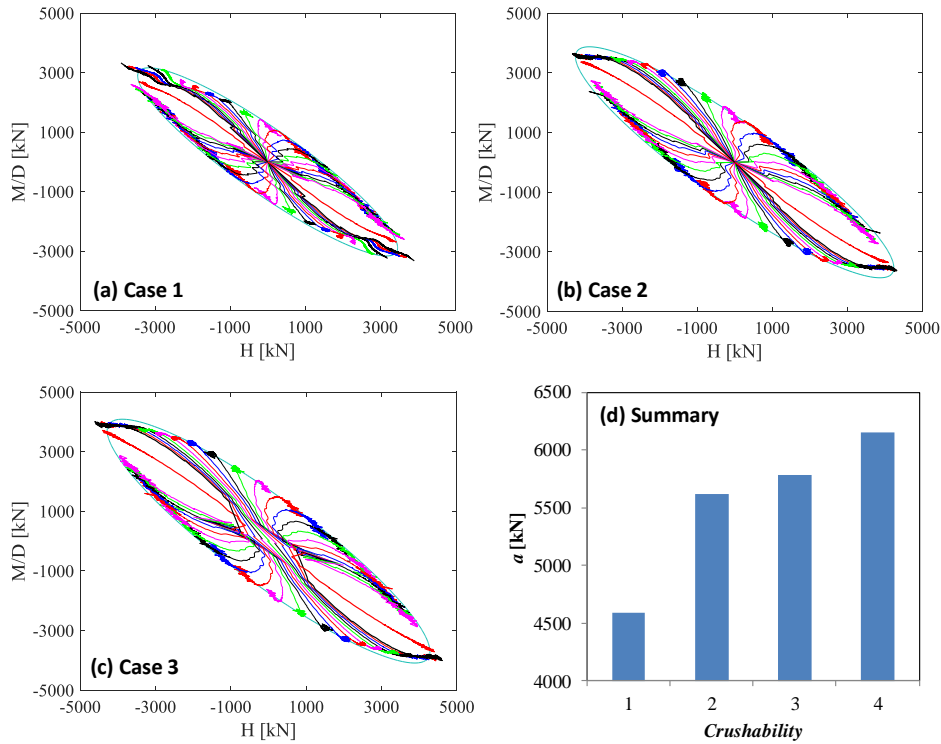


Figure 21 Failure envelopes in the  $H$ - $M$  plane for different sand grain crushabilities: (a) easy crushing, (b) medium crushing, (c) hard crushing, and (d) ellipse size  $a$  versus crushability

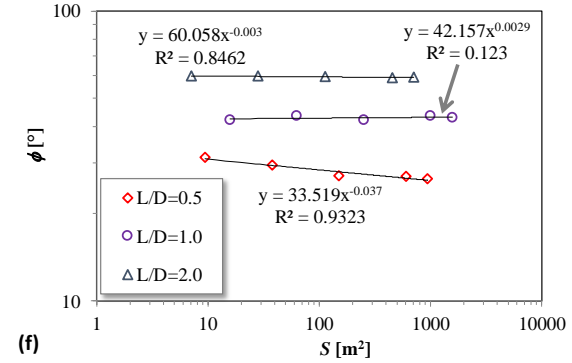
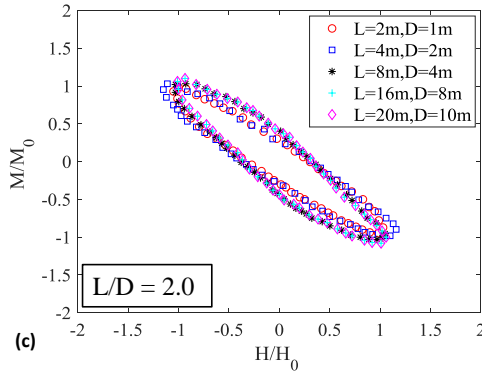
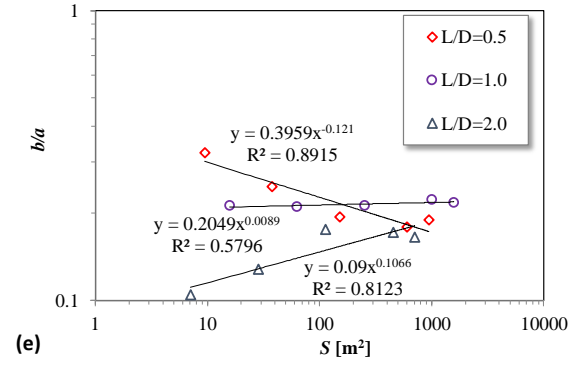
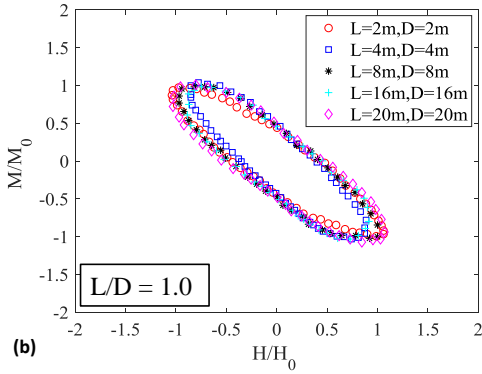
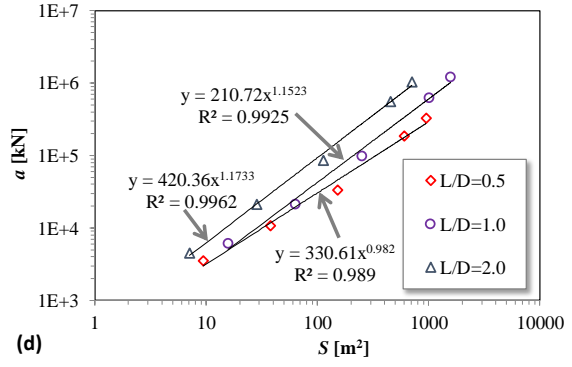
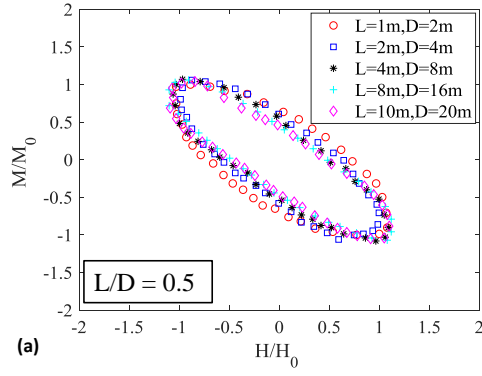


Figure 22 Normalized failure envelopes in the  $H$ - $M$  plane for different geometry sizes: (a)  $L/D = 0.5$ , (b)  $L/D = 1.0$ , (c)  $L/D = 2.0$  and plot of the failure envelope characteristic measures versus the contact surface area  $S$  (d) ellipse size  $a$ , (e) ratio  $b/a$ , and (f) inclination angle  $\phi$

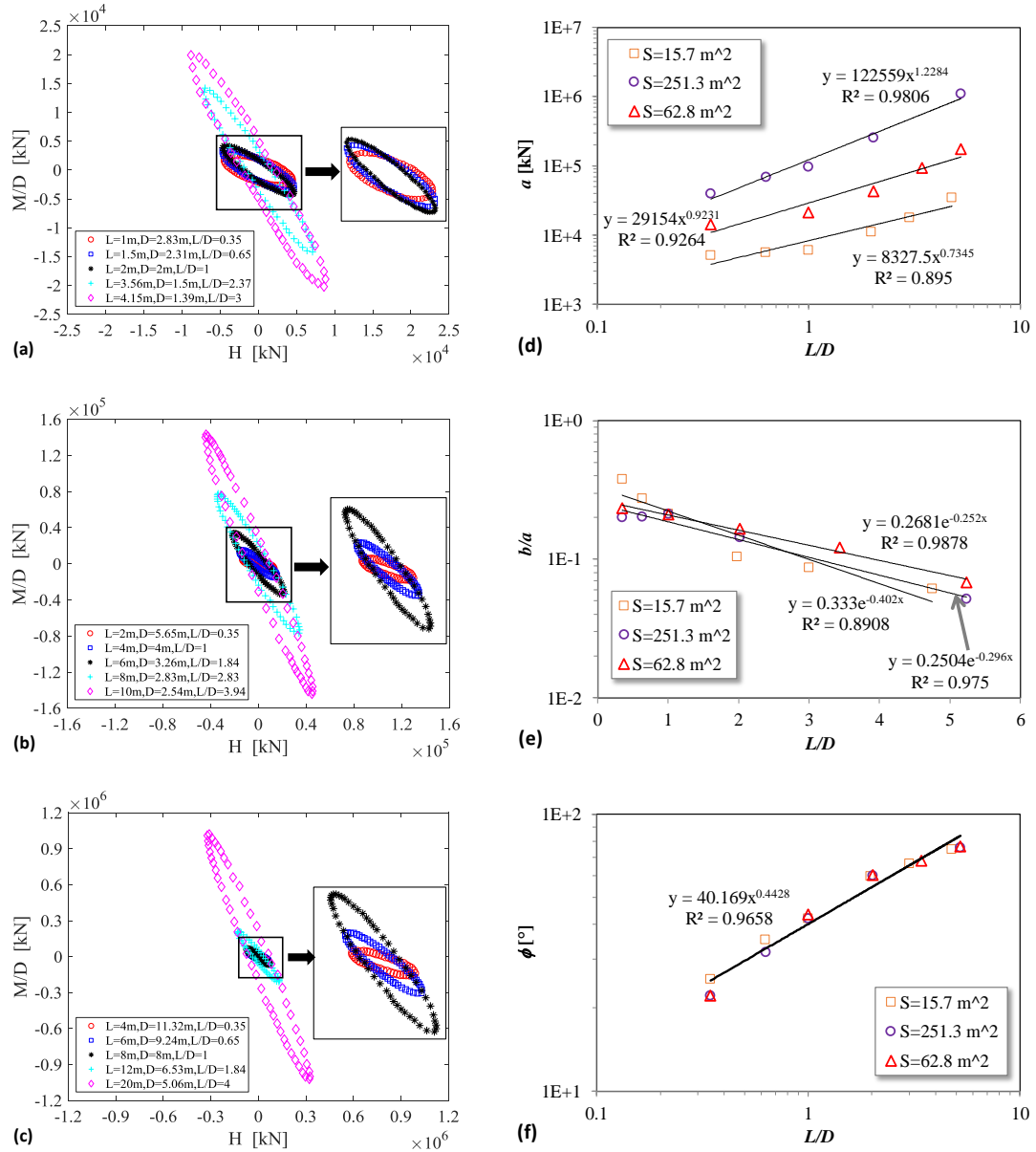


Figure 23 Failure envelopes in the  $H$ - $M$  plane for different geometry sizes: (a)  $2 \times 2$  m, (b)  $4 \times 4$  m, (c)  $8 \times 8$  m, and plot of the failure envelope characteristic measures versus the aspect ratio  $L/D$ : (d) ellipse size  $a$ , (e) ratio  $b/a$ , and (f) inclination angle  $\phi$

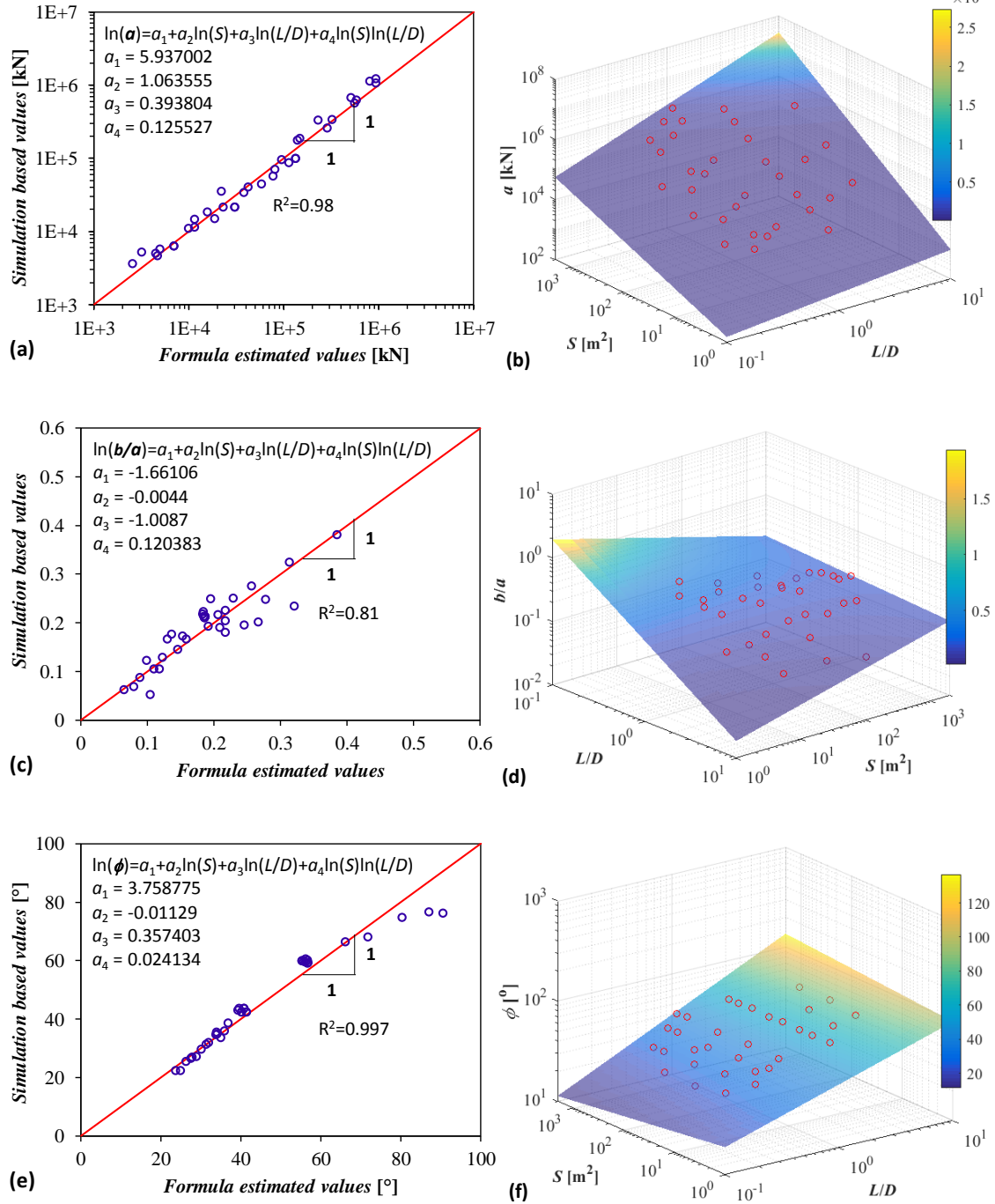


Figure 24 Comparison between numerically obtained characteristic measures and formula estimated values for:  
 (a) size of ellipse  $a$  (b) 3D plot of  $a$  versus  $S$  and  $L/D$ , (c)  $b/a$  with (d) 3D plot of  $b/a$  versus  $S$  and  $L/D$ , and  
 (e) inclination angle  $\phi$  with (f) 3D plot of  $\phi$  versus  $S$  and  $L/D$

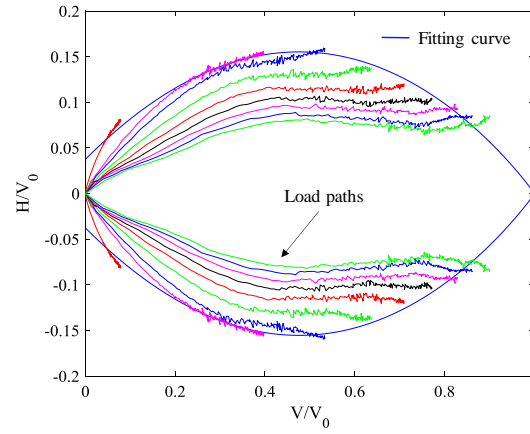


Figure 25 Numerical results for various load paths and approximate failure envelope in  $H$ - $V$  plane

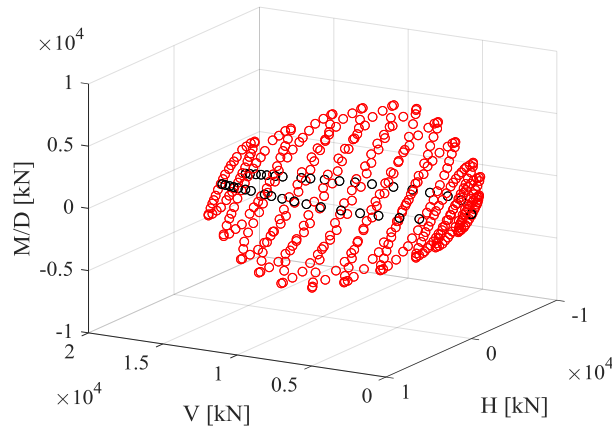


Figure 26 Failure envelope in the three-dimensional  $H$ - $M$ - $V$  space (numerical simulations)

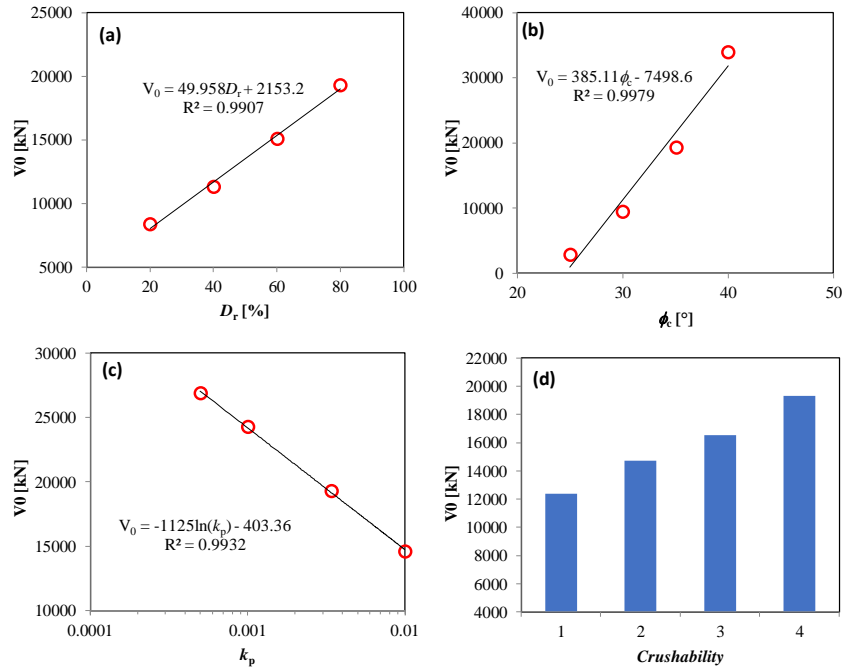


Figure 27 Relationship between vertical bearing capacity  $V_0$  and related soil properties: (a) relative density, (b) critical friction angle, (c) plastic stiffness and (d) sand grain crushability

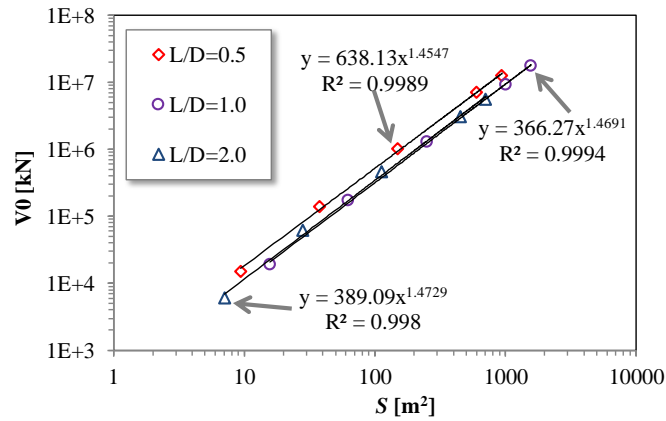


Figure 28 Vertical bearing capacity  $V_0$  versus contact surface area  $S$  for different aspect ratios  $L/D$

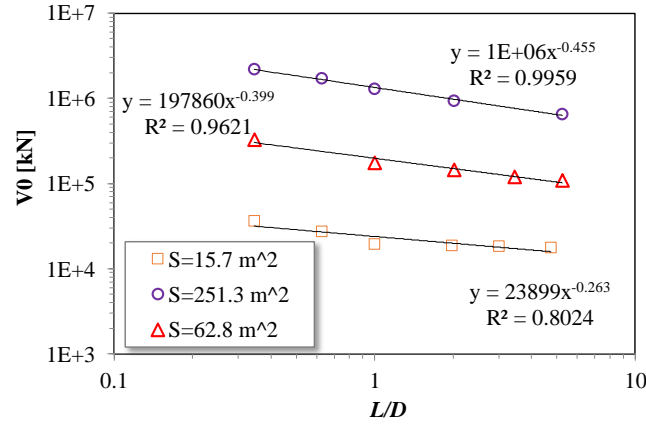


Figure 29 Vertical bearing capacity  $V_0$  versus aspect ratio  $L/D$

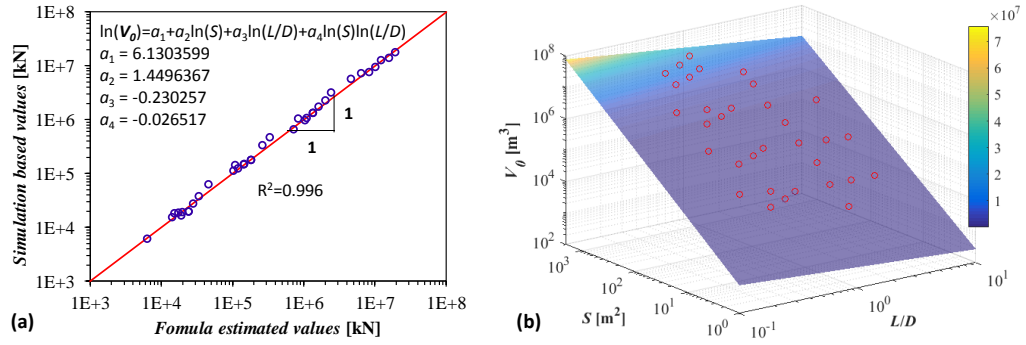


Figure 30 (a) Comparison between the vertical bearing capacity  $V_0$  and the formula estimated  $V_0$ , and (b) 3D plot of the correlation between  $V_0$ , the contact surface area  $S$  and the aspect ratio  $L/D$

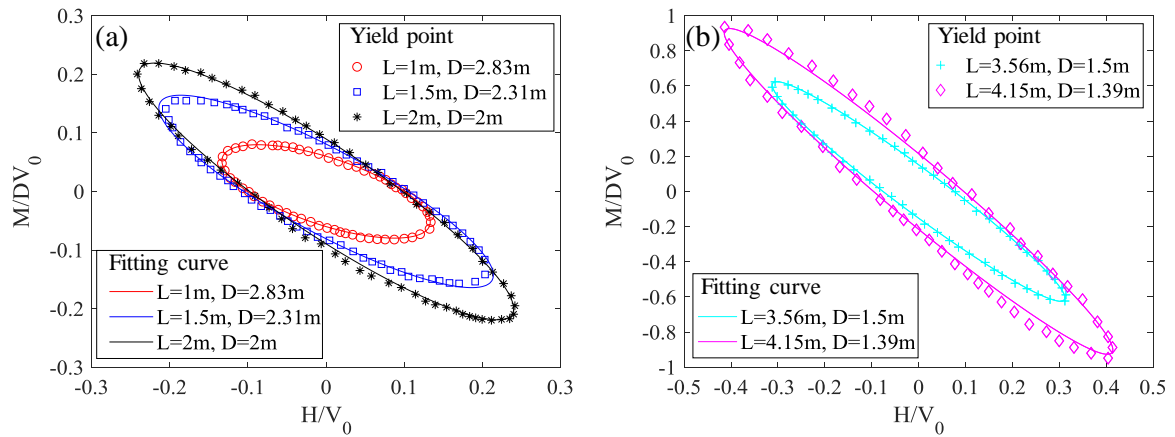


Figure 31 Comparison of fitted curves by the analytical equation and numerical results for different aspect ratios:

(a)  $L/D=0.35, 0.65$  and  $1$ , (b)  $L/D=2.37$  and  $3$



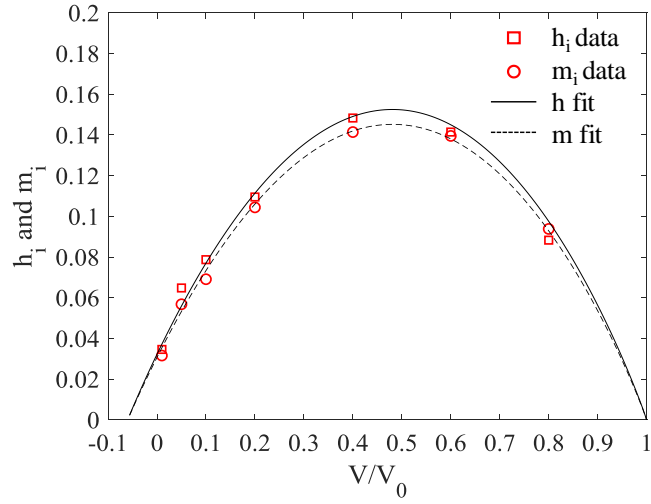


Figure 32 Intersection points  $h_i$  and  $m_i$  as a function of the normalized vertical load  $V/V_0$

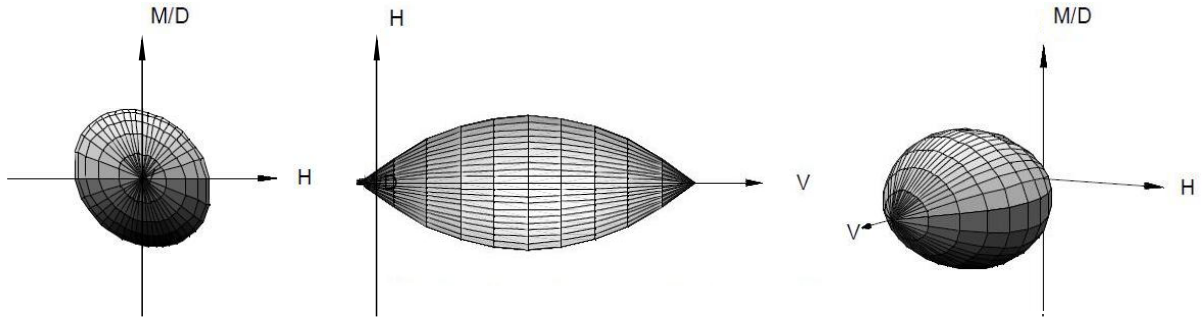
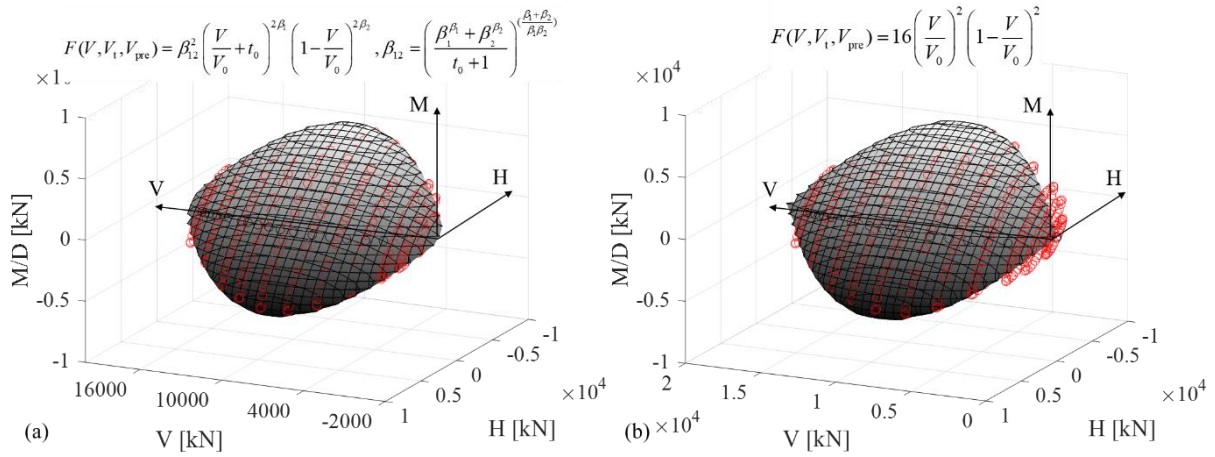


Figure 33 Illustration of the yield surface shaped as a parabola and inclined ellipse in the  $(V, M/D, H)$  load space



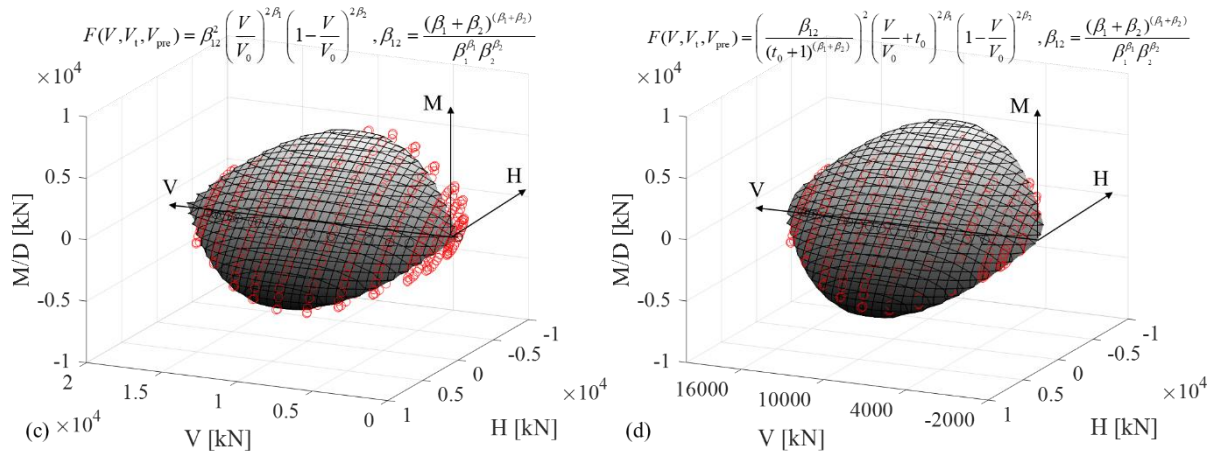


Figure 34 Numerical yield points fitted by the three-dimensional failure envelopes based on (a) Eq. (12), (b) Gottardi et al. (1999), (c) Byrne and Houlsby (1999) and (d) Villalobos et al. (2009)